

How the Galaxy–Halo Connection Depends on Large-Scale Environment

JOHN F. WU,^{1,2} CHRISTIAN KRAGH JESPERSEN,³ AND RISA H. WECHSLER^{4,5}

¹*Space Telescope Science Institute, 3700 San Martin Dr, Baltimore, MD 21218*

²*Department of Physics & Astronomy, Johns Hopkins University, 3400 N Charles St, Baltimore, MD 21218*

³*Department of Astrophysical Sciences, Princeton University, Princeton, NJ 08544, USA*

⁴*Kavli Institute for Particle Astrophysics and Cosmology and Department of Physics, 452 Lomita Mall, Stanford University, Stanford, CA 94305, USA*

⁵*SLAC National Accelerator Laboratory, 2575 Sand Hill Road, Menlo Park, CA 94025, USA*

ABSTRACT

We investigate the connection between galaxies, dark matter halos, and their large-scale environments with Illustris TNG300 hydrodynamic simulation data. We predict stellar masses from subhalo properties to test two types of machine learning (ML) models: Explainable Boosting Machines (EBMs) with simple galaxy environment features and $\mathbb{E}(3)$ -invariant graph neural networks (GNNs). The best-performing EBM models leverage spherically averaged overdensity features on 3 Mpc scales. Interpretations via SHapley Additive exPlanations (SHAP) also suggest that, in the context of the TNG300 galaxy–halo connection, simple spherical overdensity on ~ 3 Mpc scales is more important than cosmic web distance features measured using the DisPerSE algorithm. Meanwhile, a GNN with connectivity defined by a fixed linking length, L , outperforms the EBM models by a significant margin. As we increase the linking length scale, GNNs learn important environmental contributions up to the largest scales we probe ($L = 10$ Mpc). We conclude that 3 Mpc distance scales are most critical for describing the TNG galaxy–halo connection using the spherical overdensity parameterization but that information on larger scales, which is not captured by simple environmental parameters or cosmic web features, can further augment these models. Our study highlights the benefits of using interpretable ML algorithms to explain models of astrophysical phenomena, and the power of using GNNs to flexibly learn complex relationships directly from data while imposing constraints from physical symmetries.

Keywords: Large-scale structure of the universe (902), Galaxy dark matter halos (1880), Galaxy evolution (594), Astrostatistics techniques (1886), Hydrodynamical simulations (767)

1. INTRODUCTION

Galaxies form and co-evolve in tandem with their dark matter halos over cosmic timescales. Although this galaxy–halo connection has been characterized using detailed cosmological hydrodynamic simulations, many important trends can be described via simple relationships and models. For example, a galaxy’s stellar mass M_* scales with its dark matter halo mass M_{halo} , and this stellar-to-halo mass relation (SHMR) depends on whether the galaxy resides in a central or satellite subhalo.

The paper addresses two questions about large-scale galaxy environment and its impact on the galaxy–halo

connection. First, what is the optimal length for quantifying large-scale environment? Second, can a graph neural network (GNN) outperform ML models that are provided spherical overdensity and/or cosmic web features, thereby showing that these summary statistics are incomplete? We will answer these questions by measuring how well various algorithms can estimate baryons purely from dark matter halo properties, i.e., recover the galaxy–halo connection for a single hydrodynamic simulation.

One way to model the galaxy–halo connection is via subhalo abundance matching (SHAM), a non-parametric mapping between stellar mass and subhalo mass (e.g., Vale & Ostriker 2004). The galaxy–halo connection can also be formulated using other kinds of models, such as halo occupation distribution HOD or

conditional luminosity function (CLF) approaches (e.g., Peacock & Smith 2000; Seljak 2000; Benson et al. 2000; Berlind & Weinberg 2002; Yang et al. 2003; Kravtsov et al. 2004; Zheng et al. 2005). For a comprehensive overview of the galaxy–halo connection, and outstanding questions, see the review by Wechsler & Tinker (2018).

We investigate the galaxy–halo connection through machine learning (ML) models that can exploit and quantify the impacts of large-scale galaxy environment. Previous studies have shown that ML models trained on hydrodynamic simulation outputs can more accurately populate baryonic properties onto dark matter subhalos than SHAM or HOD models (e.g., Kamdar et al. 2016; Agarwal et al. 2018; Calderon & Berlind 2019; Zhang et al. 2019; Moster et al. 2021; Mohammad et al. 2022; Wu & Jespersen 2023; Chuang et al. 2023).

Galaxy physical properties and clustering properties depend on variables beyond than halo mass, a phenomenon known as assembly bias. At given halo mass, halos that formed earlier or have higher mass concentrations tend to cluster more strongly and are more often populated with central galaxies (e.g., Wechsler et al. 2002; Sheth & Tormen 2004; Wechsler et al. 2006; Wang et al. 2007; Hahn et al. 2009; Mao et al. 2018; Zehavi et al. 2018). Incorporating a subhalo’s merger history is helpful for predicting baryons from dark matter subhalos. For example, the galaxy–halo connection can be augmented by tracking satellite properties at time of accretion (Conroy et al. 2006; Christensen et al. 2023), by including merger history parameters (Chuang & Lin 2023; Hausen et al. 2023), or by directly using the merger tree (Jespersen et al. 2022; Chuang et al. 2023).

Assembly bias is also sometimes also studied through the lens of galaxy environment. The importance of galaxy environment beyond a central galaxy’s virial radius has been debated (e.g., Kauffmann et al. 2004; Blanton et al. 2006; Weinmann et al. 2006), but observational evidence for large-scale correlations in galaxy properties has been mounting with deeper and wider galaxy surveys. While observations have revealed that redder galaxies preferentially populate overdense environments (e.g., Dressler 1980; Hogg et al. 2003; Blanton et al. 2005), the physical processes that produce such correlations beyond galaxies’ virial radii are not yet well understood (e.g., Wechsler & Tinker 2018; Zehavi et al. 2018). For example, galaxy colors and star formation rates appear to be synchronized across ~ 3 Mpc scales (“two-halo” galactic conformity, see, e.g., Kauffmann et al. 2013; Olsen et al. 2021; Olsen & Gawiser 2023). Galactic conformity has also been reproduced in simulations and semi-analytic models, although these studies sometimes disagree about the physical processes

responsible for the signal (Somerville et al. 2008; Hearin et al. 2015, 2016; Lacerna et al. 2018, 2022; Ayromlou et al. 2023).

There are several ways to parameterize a galaxy’s surroundings. One of the simplest methods is to define an average overdensity, δ . Variations of this parameter can measure the total mass or galaxy number density within a specified radius, L (e.g., Blanton et al. 2006; Tinker et al. 2008). This definition of overdensity is equivalent to a convolution with a spherical “top-hat” filter over the mass or number counts. Other works measure overdensity using the distance to the N th nearest neighbor (e.g., Peng et al. 2010; Woo et al. 2013).

A constant length scale may not robustly characterize galaxy environment; galaxy large-scale structure is dynamic and cannot be fully captured by the positional configuration of galaxies in a single cosmic snapshot. Therefore, detecting the *persistent* cosmic web structures to characterize galaxy environments is crucial. One of the most well-known methods, DisPerSE, relies on topological data analysis to identify filaments and nodes in the cosmic web (see, e.g., Sousbie 2011; Galárraga-Espinosa et al. 2020; Hasan et al. 2023; Wang et al. 2023). The persistent cosmic web can be essential for understanding large-scale structure beyond mass distributions at a single snapshot; for example, galaxy spins are aligned with the cosmic web in simulations (e.g., Pichon et al. 2011; Laigle et al. 2015).

We focus on modeling the $z = 0$ relationship between galaxy stellar mass and dark matter subhalo properties because it is an important theoretical prediction from Λ CDM. In particular, the SHMR is sensitive to many physical processes at both the low- and high-mass ends and has been well-calibrated in hydrodynamic simulations (e.g., Somerville & Davé 2015; Bullock & Boylan-Kolchin 2017). Moreover, a galaxy’s stellar mass assembly also depends on physics that occurs over very different timescales (see, e.g., Iyer et al. 2020), which must be captured in the ML models even though we do not directly account for the assembly history. Therefore, we aim to understand how galaxy environment impacts a ML model’s ability to estimate present-day stellar mass from $z = 0$ dark matter subhalo catalogs.

The layout of our paper is as follows. In Section 2, we describe the TNG300 simulation data used in this work. In Section 3, we introduce the algorithms in our analysis, including Explainable Boosting Machines and Graph Neural Networks. We present our results in Section 4, and interpret the models in Section 5. We discuss the findings in Section 6. Finally, we present our conclusions in Section 7. Several methodological details, model results, and discussions can be found in Appendix A.

2. DATA

Our data set is based on SUBFIND subhalo catalogs (Springel et al. 2001) from the Illustris TNG300-1 cosmological hydrodynamic simulations (hereafter, TNG300, Nelson et al. 2019; Pillepich et al. 2019). The TNG300 simulations adopted the Planck Collaboration et al. (2016) cosmology with $H_0 = 67.74 \text{ km s}^{-1} \text{ Mpc}^{-1}$. We select subhalos from TNG300 matched to their counterpart subhalos from the TNG300-1-Dark (dark matter only) simulation. For our catalogs, subhalos must be detected by both the Sublink (Rodríguez-Gomez et al. 2015) and LHalotree (Nelson et al. 2015) algorithms, which ensures a high level of confidence that the subhalos are well-resolved and matched correctly (but may result in some incompleteness). By imposing this matching criterion, we remove 4.5% of subhalos from the catalog.

We remove all flagged subhalos (SubhaloFlag != 0), as well as all subhalos with fewer than 50 star particles, halo masses below $\log(M_{\text{halo}}/M_{\odot}) = 11$, or stellar masses below $\log(M_{\star}/M_{\odot}) = 9$. For each subhalo, we use the 3d positions \mathbf{x} , 3d velocities \mathbf{v} , logarithmic halo mass M_{halo} , maximum circular velocity V_{max} , and whether the subhalo is a central or satellite, $\Gamma_{\text{cen}} \in \{0, 1\}$. After applying these cuts, 76.1% of the 208,037 remaining subhalos are centrals (in the dark matter only simulation).

We compute the total logarithmic halo mass within a radius of length L for each subhalo, which we define as the spherical local overdensity δ_L .¹ We also augment the subhalo catalog with a table of cosmic web features generated for the TNG300 simulations (Duckworth et al. 2019) using the DisPerSE code (Sousbie 2011). Specifically, we employ their catalog of distances to the nearest void, 1-saddle point, 2-saddle point, node, and skeleton. In astronomy terminology, 1-saddle points are also known as walls, 2-saddle points are filaments, nodes are clusters or groups, and the skeleton is simply any of the above cosmic web features. These cosmic web parameters are discussed further in Section 3.1.2.

3. METHODOLOGY

To probe the impact of galaxy environment on the modeled galaxy–halo connection, we rely on Explainable Boosting Machines (EBMs; Section 3.1) and GNNs (Section 3.2). We train a base model, EBM-base, which takes as input the halo mass, M_{halo} , maximum circular velocity, V_{max} , and whether or not the subhalo is a central or satellite, Γ_{cen} . We train another model, EBM-

DisPerSE, which extends the base model inputs using five features corresponding to distances from persistent cosmic web structures measured using the DisPerSE code. Finally, we train another set of models, EBM-overdensity, which consists of the base model augmented with subhalo mass overdensities, δ_L , averaged over a spherical volume with radius $L \text{ Mpc}$.² We test values of $L \in \{0.3, 0.5, 1, 1.5, 2, 2.5, 3, 3.5, 4, 5, 7.5, 10\} \text{ Mpc}$. For the GNN models, we test the same set of linking lengths used to connect subhalos during the construction of the cosmic graph. The GNN learns an optimal combination of flexible summary statistics to represent environmental information on scales up to L .

Readers who wish to skip over the details of our methodology may still wish to read about the baseline EBM model (Section 3.1.1), the DisPerSE cosmic web features (Section 3.1.2), and the spherical overdensity features (3.1.3). We also present an overview of the GNN inputs and model architecture in Figure 1. Additional GNN details are supplied in Appendix A.

3.1. Explainable Boosting Machines

Before we introduce EBMs, we begin by describing simpler interpretable models. First, let us consider *generalized linear models*:

$$y = \beta_0 + \sum_{n=1}^N \beta_n x_n, \quad (1)$$

where the learnable model coefficients β_1, \dots, β_n are linear with the input features x_1, \dots, x_n . The model is interpretable because these coefficients can be regarded as feature importances (if the inputs span the same domain). However, generalized linear models are often not expressive enough to fit complex relations between the independent and dependent variables when the underlying functional form is unknown. This results in inaccurate predictions and erroneous interpretations of the best-fit coefficients.

We can extend generalized linear models by making predictions using non-linear functions, $f_n(x_n)$:

$$y = \beta_0 + \sum_{i=1}^N f_i(x_i). \quad (2)$$

These *generalized additive models* (Hastie & Tibshirani 1986) can more flexibly fit combinations of input fea-

¹ This is equivalent to convolving with a spherical top-hat filter with radius L .

² Note the slight abuse of notation: we use L to define distance scales for both the spherically averaged overdensity, as well as the graph connectivity later. These definitions are physically distinct. However, as we will see, both methods arrive at similar characteristic length scales, so we use L in both contexts.

tures. In practice, splines or other basis functions can be used for the functions f_n .

Generalized additive models can be extended even further by allowing pairwise interactions (Lou et al. 2013):

$$y = \beta_0 + \sum_{n=1}^N f_n(x_n) + \sum_{n=1}^N \sum_{m=n+1}^N f_{mn}(x_m, x_n), \quad (3)$$

These generalized additive models with pairwise interactions can not only offer interpretable model components but also produce competitive results compared to other popular ML algorithms such as random forests (Breiman 2001), gradient boosted trees (Friedman 2001), or neural networks (e.g., LeCun et al. 1989).

EBMs are generalized additive models with pairwise interactions, where the non-linear functions are binned look-up tables. EBMs are also optimized using a specific routine; to train them, we iteratively build the model described in Equation 3 one feature at a time and minimize the residuals at each step (i.e. gradient boosting). We implement and train the EBM using the `ExplainableBoostingRegressor` class from the `InterpretML` Python module (Nori et al. 2019). The model has no trouble converging on a solution to fit stellar masses from halo properties. To maximize performance, we set the number of bins per feature to 50,000 and the number of interactions to 32, which we found to be effective via a quick hyperparameter scan.

3.1.1. The EBM-base model

The aim of the EBM-base model is to provide a strong baseline estimate of the galaxy–halo relation using only simple summary statistics. Since the EBM models use one- and two-dimensional look-up tables for the f_n and f_{mn} functions in Equation 3, respectively, they are similar to conditional abundance matching models. The EBM-base can learn univariate and pair-wise interactions between the input variables M_{halo} , V_{max} , and Γ_{cen} .

3.1.2. The EBM-DisPerSE model

We also include cosmic web features based on discrete Morse and persistence theories that quantify the large-scale topology (e.g., Pogosyan et al. 2009; Pichon et al. 2011), produced from the `DisPerSE` code (Sousbie 2011). Persistence quantifies the robustness of topological structures to local perturbations. In the context of galaxies and large-scale structure, higher persistence results in a more reliable cosmic web skeleton while filtering out small-scale features. Significant work has shown that `DisPerSE` is essential for extracting and characterizing the cosmic web in both simulated and observed data (e.g., Bonjean et al. 2020; Galárraga-Espinosa et al.

2020; Malavasi et al. 2020; Rost et al. 2021; Galárraga-Espinosa et al. 2022; Hasan et al. 2023; Hoosain et al. 2024).

We use five `DisPerSE` features that have been run on the TNG300 catalogs and published online:³ `d_minima`, `d_saddle_1`, `d_saddle_2`, `d_node`, `d_skel` (Duckworth et al. 2019, 2020, see also Section 2). These features quantify each subhalo’s position relative to persistent large-scale structures such as voids, walls, filaments, clusters, and the nearest portion of the cosmic web skeleton, respectively. Given `DisPerSE`’s ability to encode information about the cosmic web, we expect these features to be critical for learning an improved galaxy–halo relation. We train the EBM-`DisPerSE` model to predict stellar masses using the base subhalo features (M_{halo} , V_{max} , Γ_{cen}) supplemented by the five cosmic web distance features.

3.1.3. The EBM-overdensity models

For the EBM-overdensity model, we augment the base subhalo features (M_{halo} , V_{max} , Γ_{cen}) with the averaged spherical overdensity on L scales, δ_L . Here, the spherical overdensity is computed as the summed mass of all subhalos within a radius of L Mpc, which serves as a simple measure of the large-scale environment (Blanton et al. 2006; Tinker et al. 2008). We retrain and cross-validate EBM-overdensity models while varying $L \in \{0.3, 0.5, 1, 1.5, 2, 2.5, 3, 3.5, 4, 5, 7.5, 10\}$ Mpc to probe a wide range of length scales. Length scales larger than 10 Mpc are poorly sampled in TNG300, so we restrict our analysis to the range of galaxy environments on 0.3 to 10 Mpc length scales.

3.2. Graph Neural Networks

A graph is a mathematical structure comprising a set of objects and the relationships between those objects. For each TNG300 sub-box, we construct a cosmic graph to represent all subhalos and their pair-wise relationships. Subhalos are represented as nodes, and pairs of subhalos are connected with edges if they are separated by less than L , the linking length. We do not permit nodes to connect to themselves (i.e., no self-loops). The ordering of subhalos is irrelevant, as graphs are invariant (and their nodes are equivariant) to permutations of the node indices. We will typically denote nodes or node properties using a single index, such as i , and edges or edge properties with two indices, such as ij . An example graph is shown in Figure 1 panel (a).

³ A persistence of 4σ was used to generate these catalogs. For more details, see the code here: <https://github.com/illustrisng/disperse.TNG>.

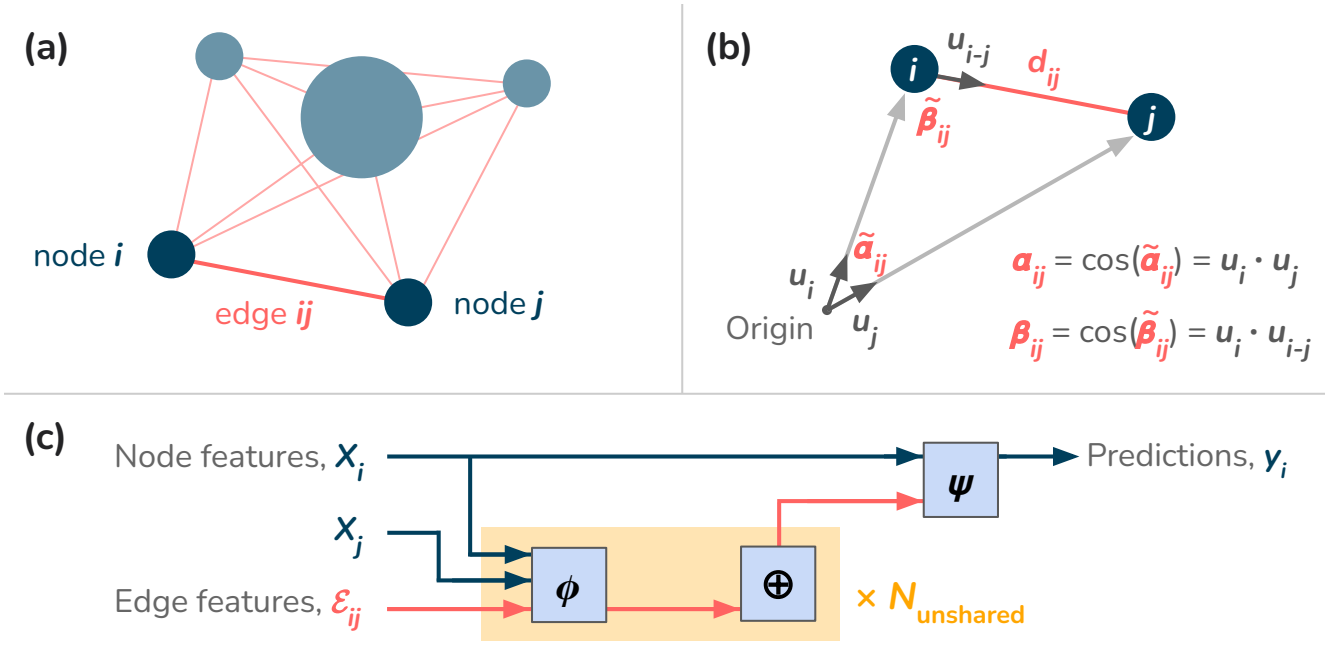


Figure 1. A schematic showing the graph features and GNN model. Nodes and node features are shown in blue, while edges and edge features are shown in red. (a) We depict a toy example of five subhalos (nodes) fully connected by edges; self-loops are not shown here. Two nodes (i and j) and the edge connecting them (ij) are highlighted. (b) $\mathbb{E}(3)$ -invariant edge features are constructed by selecting an (arbitrary) origin and a pair of nodes, and computing the distance d_{ij} , inner product between unit vectors u_i and u_j , and inner product between unit vectors u_i and u_{i-j} . (c) We show a flow diagram for the GNN, which receives inputs on the left and predicts outputs on the right. The graph interactions are composed of ϕ and ψ , learnable functions parameterized by neural networks, and \oplus , a permutation-invariant function that aggregates edge information onto a single node. We use multiple “unshared” edge layers that compute features in parallel. See text for more details.

Statistical and ML models can harness the symmetries and inductive biases of mathematical graphs and efficiently learn robust representations (e.g., Battaglia et al. 2018). One important characteristic of graphs and sets is permutation invariance: the data have no natural ordering, so shuffling the node indices has no effect. Additionally, subhalos reside in a $3d$ space and obey geometric constraints, i.e., they are invariant under the $\mathbb{E}(3)$ group action. GNNs can learn robust representations from fewer data examples by imposing the graph structure and various symmetries as *constraints* on the model (Villar et al. 2021; Geiger & Smidt 2022). These symmetries are due to physically invariant or equivariant phenomena, and models that have such symmetries inherent to them can learn more efficiently. In Section 6.6, we discuss the inductive biases of GNNs in more detail. We also refer the interested reader to Battaglia et al. (2018), Schlichtkrull et al. (2018), and Bronstein et al. (2021), which describe GNNs and geometric deep learning at a high level.

3.2.1. Graph features

We can ascribe features to graph nodes and edges. For nodes, we only use the subhalo mass, maximum cir-

cular velocity, and whether the subhalo is a central or satellite. Importantly, we do not assign positions or velocities as node features since they depend on the frame of reference. Instead, we construct edge features that are fully invariant under the $\mathbb{E}(3)$ group action: three features based on pairs of node positions and three features based on pairs of node velocities. Our choice of architecture and feature set ensures that our model is an $\mathbb{E}(3)$ -invariant GNN (for more, see e.g., Satorras et al. 2021; Villar et al. 2021), and differs from the model used by Wu & Jespersen (2023) because we include invariant features in velocity space.

To create these edge features, we follow Villanueva-Domingo & Villaescusa-Navarro (2022), and first define unit vectors $\mathbf{u}_i \equiv (\mathbf{x}_i - \bar{\mathbf{x}}) / \|\mathbf{x}_i - \bar{\mathbf{x}}\|$ relative to the center of the distribution $\bar{\mathbf{x}}$ (which we treat as an arbitrary origin). We then create the following features between nodes i and j : the squared Euclidean distance $d_{ij} \equiv \|\mathbf{x}_i - \mathbf{x}_j\|^2$, the inner product $\alpha_{ij} \equiv \mathbf{u}_i \cdot \mathbf{u}_j$, and the inner product $\beta_{ij} \equiv \mathbf{u}_i \cdot \mathbf{u}_{i-j}$.⁴ If a triangle is drawn using the origin and nodes i and j , then α_{ij} and β_{ij} can

⁴ \mathbf{u}_{i-j} is the unit vector toward $\mathbf{x}_i - \mathbf{x}_j$.

be geometrically interpreted as the cosine of the angles opposite and next to the edge ij . Figure 1 panel (b) illustrates these edge features.

3.2.2. GNN architecture

As discussed in the previous section, we first create our cosmic graph with node features

$$X_i = (M_{\text{halo},i}, V_{\text{max},i}, \Gamma_{\text{cen},i}), \quad (4)$$

and edge features

$$\mathcal{E}_{ij} = \left(d_{ij}^{(\mathbf{x})}, \alpha_{ij}^{(\mathbf{x})}, \beta_{ij}^{(\mathbf{x})}, d_{ij}^{(\mathbf{v})}, \alpha_{ij}^{(\mathbf{v})}, \beta_{ij}^{(\mathbf{v})} \right), \quad (5)$$

between any two nodes that are separated by less than the linking length, L . These features are passed through our GNN, which is trained to predict

$$y_i = (M_\star, \sigma_{M_\star}), \quad (6)$$

i.e., the stellar mass and the scatter on stellar mass for every subhalo. A schematic of our GNN architecture is shown in Figure 1 panel (c), while details are presented in Appendix A.

Our GNN is parameterized by learnable functions ψ and ϕ , which are multilayer perceptrons (MLPs). We also use $N_{\text{unshared}} = 8$ MLPs in parallel to learn interactions on graph edges, and these are known as “unshared” layers. These unshared layers are indexed by $\ell = \{1, 2, \dots, N_{\text{unshared}}\}$.

For some edge indexed by ij , we provide node features X_i, X_j , and edge features \mathcal{E}_{ij} as inputs to a function, ϕ , which produces a hidden state $e_{ij}^{(\ell)}$ per unshared layer:

$$e_{ij}^{(\ell)} = \phi^{(\ell)}(X_i, X_j, \mathcal{E}_{ij}). \quad (7)$$

The MLP $\phi^{(\ell)}$ comprises two linear layers, each with $N_{\text{hidden}} = 64$ hidden neurons, LayerNorm, and then SiLU activation, and outputs a latent vector with $N_{\text{latent}} = 16$ dimensions via a final linear layer.

An aggregation function \oplus_j operates on all edge hidden states e_{ij} that connect to node i , i.e., it pools over all neighboring j . Here we define \oplus to be a multi-pooling operator, which concatenates the outputs of sum-pooling, mean-pooling, and max-pooling functions. Since these pooling functions are invariant to permutations, the multi-pooling operator is also permutation invariant.

The function ψ receives a concatenated set of N_{unshared} features pooled into node i , as well as the node variable X_i , to make predictions:

$$y_i = \psi \left(X_i, \left\{ \oplus_j \left(e_{ij}^{(\ell)} \right) \right\}_{(\ell)} \right). \quad (8)$$

The function ψ is composed of three parts: ψ_1 , which ingests all pooled edge features and returns a 16-dimensional latent node state, ψ_2 , which ingests the latent node state and outputs a 16-dimensional latent node state, and ψ_3 , which ingests the concatenated outputs of ψ_1 and ψ_2 and produces the final prediction. Each of ψ_1, ψ_2, ψ_3 have two hidden layers, each with $N_{\text{hidden}} = 64$ hidden neurons, LayerNorm, and SiLU activations, and a final linear layer; they only differ in the number of input and output neurons.

We note that a deeper neural network can be constructed by sequentially stacking GNN layers. For example, if we instead predicted another node latent state and allowed a second round of interactions using learned functions across the graph of node and edge latent states, then we could represent higher-order interactions up to a length scale $2L$. Increased GNN depth would enable improved performance due to enhanced internal representations of neighboring galaxies before the final layer. Indeed, several works find that increasing the number of sequential GNN layers can improve the predictive power (e.g., Sanchez-Gonzalez et al. 2020; Pfaff et al. 2021; Lam et al. 2022). However, we are interested in assessing the optimal linking length scale, so we only use a single GNN layer in depth, thereby restricting the receptive field to a radius of L .

3.2.3. GNN optimization procedure

The data are split into training and validation sets using $k = 3$ -fold cross-validation as follows. First, we divide the TNG300 box along the z dimension into three equal sub-volumes. We train on two sub-volumes and validate on the remaining sub-volume. The TNG300 box is periodic, so the two training sub-volumes are always contiguous. During training, we remove 10 Mpc from the box as “padding” along the z axis, which ensures that the training and validation sets are fully independent. In other words, the training sub-volume is $\sim 300 \times 300 \times 180 \text{ Mpc}^3$, while the validation sub-volume is $\sim 300 \times 300 \times 100 \text{ Mpc}^3$. We iterate over the three validation sub-volumes and concatenate the validation results to catalog predictions over the entire volume without any gaps. Results are reported as the mean and standard deviation of the three cross-validation predictions unless otherwise noted.

We divide the data into mini-batches using the Pytorch-Geometric ClusterLoader sampling strategy (Chiang et al. 2019) with 48 clusters. At each mini-batch optimization step, GNN model parameters are updated to minimize a negative log-likelihood loss:

$$\text{NLL} = \frac{1}{2b} \sum_{i=1}^b \frac{(M_{\star,i} - \hat{M}_{\star,i})^2}{\hat{\sigma}_{M_\star}^2} - \frac{1}{2} \log(\hat{\sigma}_{M_\star}^2), \quad (9)$$

Table 1. Comparison of main ML model results. We show how different models perform on estimating M_* from subhalo properties. We have selected the best environmental length scale for the GNN and EBM with spherically averaged overdensity (δ_L) models. The RMSE shown is the mean and standard deviation using $k = 3$ -fold cross-validation. The best performance is highlighted in bold.

Model	N_{features}	L_{best} (Mpc)	RMSE (dex)
SHAM- V_{max}	1	—	0.1779 ± 0.0007
EBM-base	3	—	0.1660 ± 0.0011
EBM-DisPerSE	8	—	0.1618 ± 0.0013
EBM-overdensity	4	3	0.1606 ± 0.0012
GNN	12	10	0.1499 ± 0.0017

where b is the batch size and $\hat{\sigma}_{M_*}^2$ is the predicted variance averaged over a batch. We train the GNN for 300 epochs, where an epoch represents a full pass through the training set, and then report the predicted M_* and σ_{M_*} for the validation set. We describe additional GNN architecture and training procedure details in Appendix A.

4. RESULTS: MODEL PERFORMANCE

We train the EBM-base, EBM-DisPerSE, EBM-overdensity, and GNN models to convergence, as described in the previous section. The EBM-overdensity and GNN experiments are repeated for multiple values of L , the environmental length scale. We compare the stellar mass root mean squared error (RMSE),

$$\text{RMSE} = \left(\frac{1}{N} \sum_{i=1}^N (M_{*,i} - \hat{M}_{*,i})^2 \right)^{1/2}, \quad (10)$$

as the RMSE directly quantifies the prediction accuracy.

We summarize each of the best model’s results in Table 1. For each model, we show the number of input features (N_{features}) and the optimal linking length (L_{best}). We also show results for a SHAM model that matches V_{max} to M_* , which serves as a commonly used baseline model (SHAM- V_{max} , e.g., Conroy et al. 2006). Although the EBM models outperform the SHAM- V_{max} model, the EBM performance can be further stratified: the EBM-DisPerSE and EBM-overdensity models have similar performance and surpass the EBM-base model. The GNN performance handily exceeds all others.

Figure 2 shows how stellar mass estimates depend on linking length. The EBM-base and EBM-DisPerSE

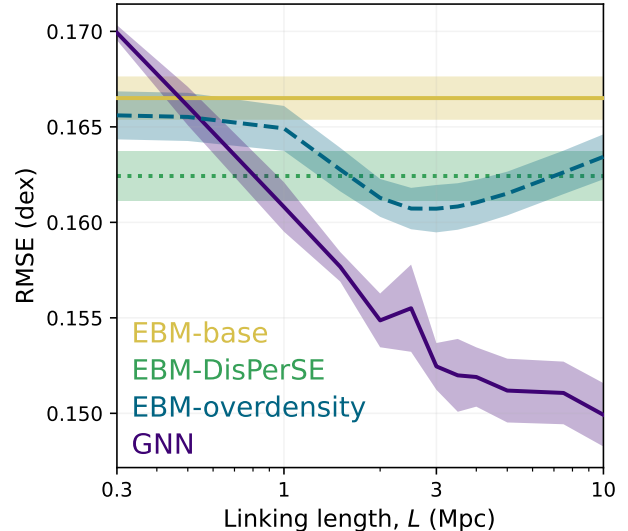


Figure 2. Stellar mass prediction errors (lower is better) for different models as a function of L . GNNs with large linking lengths perform the best. We show model performance for EBM-base (solid yellow), EBM-DisPerSE (dotted green), EBM-overdensity (dashed blue), and GNN (solid purple). Lines depict the mean root mean squared error based on $k = 3$ cross-validation, while the shaded region indicates the 1σ scatter.

models do not vary with linking length. For the EBM-overdensity, the error is minimized at a linking length of 3 Mpc. At smaller or larger scales, the average spherical overdensity is less useful for predicting stellar mass.

For the GNN model, we find that the RMSE decreases with increasing linking length until ~ 3 Mpc, and then modestly delinques at $L > 3$ Mpc (with low statistical significance). Whereas the EBM-overdensity smooths out structure at $L > 3$ Mpc and therefore loses information on smaller scales, the GNN model can continue to model environmental impacts at all scales up to L .

5. EBM MODEL INTERPRETATION

A critical part of any ML analysis is to interpret and diagnose the models (Huppenkothen et al. 2023). While there exist methods that attempt to explain the decision-making processes of “black-box” ML algorithms such as neural networks (e.g., Simonyan et al. 2014), many of these explanations are subjective and require yet another layer of interpretation. Instead, inherently interpretable models should be used when possible (see, e.g., Rudin 2019). In this section, we explore physical interpretations of our EBM model results.

5.1. Feature importance with SHAP

EBMs are interpretable because they are additive models (see Section 3.1). One can directly plot each fea-

ture’s contribution to the final prediction, although the interpretation can still be subjective. Using terminology from Equation 3, we could plot $f_i(x_i)$ versus x_i and $f_{ij}(x_i, x_j)$, marginalized over x_j , versus x_i to see how the model prediction depends on x_i , i.e., visualization can be used for *qualitative* assessments. However, here we would like to *quantitatively* interpret the importance of each feature.

To measure feature importances, we use a method called SHAP, or SHapley Additive exPlanations (Lundberg & Lee 2017). SHAP computes each feature’s contribution to the prediction based on cooperative game theory (building on another metric called Shapley values; see Shapley 1951). SHAP returns the fair distribution of additive contributions even when the model contains correlated features. Exact Shapley values can be computed using permutations of all features, which is computationally infeasible; we instead follow the standard method of randomly sampling examples with replacement ($N = 5,000$). We use the samples to approximate Shapley values and compute their SHAP feature importances. For a more technical overview of SHAP and Shapley values, we refer the interested reader to Sections 9.5 and 9.6 of Molnar (2022), and the original SHAP paper (Lundberg & Lee 2017), which describes several additional desiderata. We implement the algorithm using the `shap` Python package.

5.2. Are cosmic web features more informative than overdensity?

We cross-validate a new model, EBM-all, which includes the set of all features in EBM-DisPerSE and EBM-overdensity at $L = 3$ Mpc. In other words, the model is given the base subhalo properties, DisPerSE features, and the $\delta_{3 \text{ Mpc}}$ averaged overdensity feature. This EBM-all model achieves $\text{RMSE} = 0.1596 \pm 0.0012$, which is on par with the other top-performing EBM models but significantly less accurate than the GNN. Crucially, we can use SHAP to compare the relative importance of different model features.

We define feature importance as the mean absolute SHAP value, i.e., $\text{mean}(|\text{SHAP value}|)$. We use the mean *absolute* values because the features can add to or subtract from the final prediction, and we do not wish to average out their positive and negative contributions.

In Figure 3, we present a bar chart of the most important EBM-all features. We find that V_{max} and M_{halo} are most important for estimating M_* , followed by overdensity $\delta_{3 \text{ Mpc}}$, and then the distance to the cosmic web skeleton and nodes. Remarkably, the 3 Mpc scale overdensity is more important than the summed feature importances of *all* cosmic web distances (note that Fig-

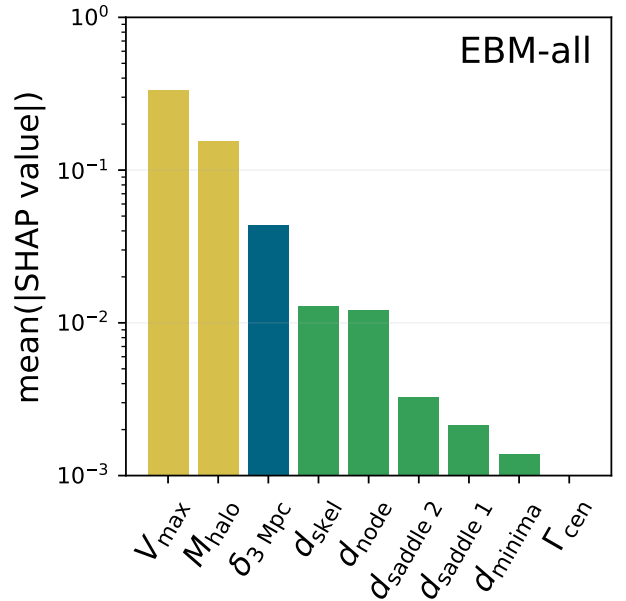


Figure 3. After V_{max} and M_{halo} , the most important EBM feature is spherical overdensity. We show SHAP values for EBM-all, which predicts stellar mass using an EBM model with base halo features (yellow), DisPerSE cosmic web features (green), and overdensity on 3 Mpc scales (blue). A higher mean absolute SHAP value indicates greater feature importance.

ure 3 shows feature importance on a logarithmic scale). This result is consistent with our earlier finding that the EBM-overdensity model at 3 Mpc outperforms the EBM-DisPerSE model (at low significance; see Figure 2). Although the DisPerSE hyperparameters are not tuned for our stellar mass prediction task, it is surprising nonetheless that the simple spherical overdensity feature outperforms the sophisticated cosmic web distance features. Our experiments show that overdensity is more informative than the DisPerSE features for predicting stellar mass from TNG300 subhalo catalogs.

5.3. What is the most important overdensity scale?

We cross-validate a new model like the EBM-overdensity model, except that we include overdensity for all $L \in \{0.3, 0.5, 1, \dots, 10\}$ Mpc as separate features. This model with all $\{\delta_L\}$ and base subhalo features ($M_{\text{halo}}, V_{\text{max}}, \Gamma_{\text{cen}}$) achieves a best $\text{RMSE} = 0.1592 \pm 0.0017$. Its performance is comparable or slightly better than the other EBM models, but still significantly worse than the GNN. Again, we can compare the feature importances for different δ_L .

In the left panel of Figure 4, we show the feature importance of δ_L for the EBM-overdensity model varied over different values of L (using $k = 3$ -fold cross-

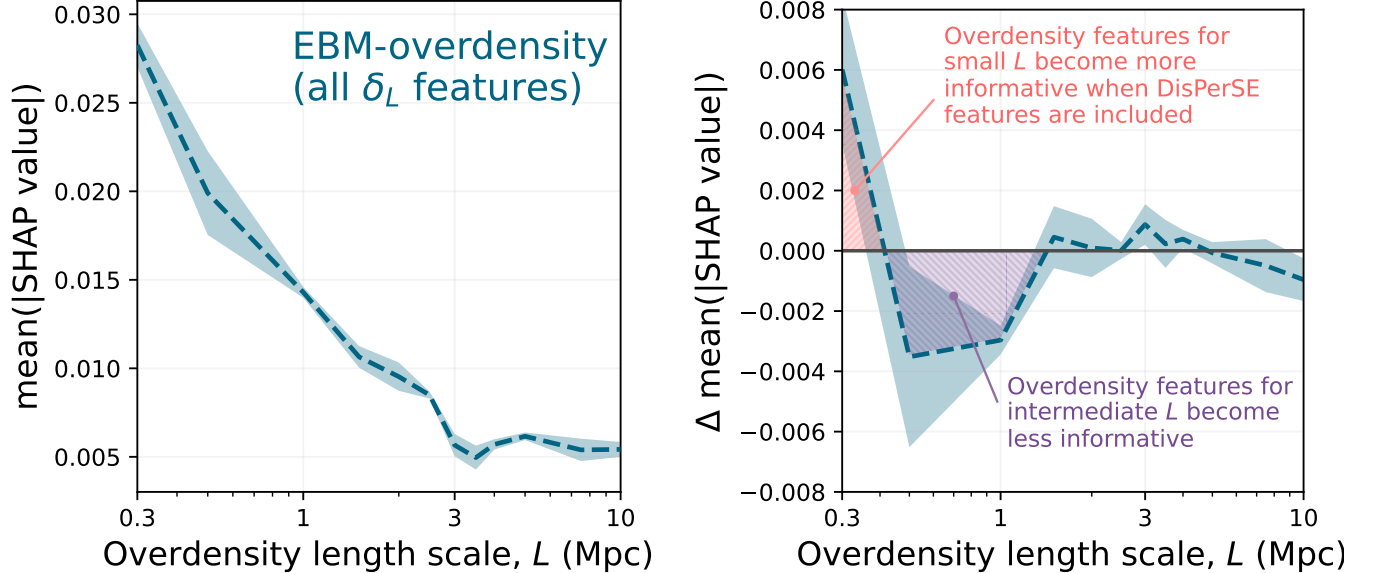


Figure 4. The most important length scales for overdensity (left), and changes to those relative importances when DisPerSE features are added (right). In the *left* panel, we show SHAP values for an EBM model that employs multiple overdensity features, each with different length scales L . SHAP values for M_{halo} and V_{max} are not shown here. In the *right* panel, we include DisPerSE parameters in addition to all overdensity and base features in the model fit and interpretation, which increases the relative importance of δ_L for small length scales, and decreases the relative importance of δ_L for intermediate length scales.

validation as before). We find that the overdensities on smaller scales are more informative in terms of SHAP values. As δ_L extends toward larger scales, the feature importance diminishes until it hits a plateau at $L \approx 3$ Mpc. Beyond $L > 3$ Mpc, the feature importance stays at a relatively low constant level. Nonetheless, SHAP indicates that there is useful information at large scales, even at 10 Mpc.

Including overdensity over progressively larger scales yields diminishing returns as we smooth out information. This trend of declining feature importance with overdensity length scale is remarkably similar to the results shown in Figure 2. Just as the GNN performance improvements diminish and the EBM-overdensity model performance suffers above $L > 3$ Mpc, Figure 4 shows that the feature contribution of δ_L also plateaus above $L > 3$ Mpc length scales. Therefore, we interpret these findings as evidence that the most important environmental overdensity in TNG300 is on 3 Mpc length scales.

To understand the interplay between spherical overdensity and cosmic web environmental parameters, we repeat the previous experiment while including DisPerSE parameters. The cross-validation RMSE is the same as before, 0.1592 ± 0.0017 , which implies that SHAP feature importances can be directly compared between the two models. Because including DisPerSE features has no impact on the cross-validation loss, the

overdensity and cosmic web features are somewhat redundant. We plot the difference in *relative* feature importance for overdensity, $\Delta \text{mean}(|\text{SHAP value}|)$, for overdensity against L in the right panel of Figure 4. We find a significant increase in relative feature importance for overdensity at ~ 0.3 Mpc scales and a decrease in relative feature importance for overdensity at $0.5 \text{ Mpc} \lesssim L \lesssim 1.5 \text{ Mpc}$ scales. These are illustrated using the figure’s red and purple shaded regions, respectively. We conclude that DisPerSE cosmic web features primarily capture information on intermediate scales (~ 1 Mpc) rather than very large scales ($\gtrsim 3$ Mpc).

6. DISCUSSION

Our EBM and GNN model results show that large-scale environmental features improve models of the TNG galaxy–halo connection by a significant margin. The EBM-base model can be augmented with cosmic web features or an averaged spherical overdensity, or better yet, a neural network can flexibly learn environmental parameters by representing subhalos as a cosmic graph. While these advanced methods are capable of lowering the RMSE for stellar mass estimates (Section 4) and for interpreting the model results (Section 5), there are many other important ways to evaluate these methods’ scientific utility. This section discusses other summary

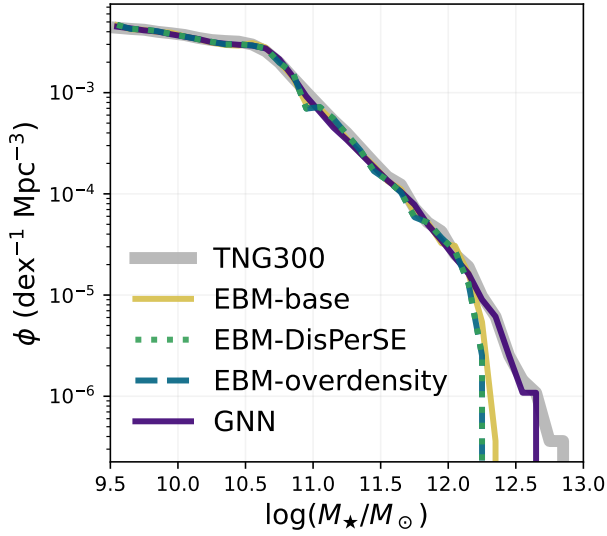


Figure 5. GNNs surpass EBMs in recovering the stellar mass function. We show stellar mass functions, ϕ , computed using the EBM and GNN methods and compared against the TNG300 simulation ground truth.

statistics and considerations in cosmology and astrophysics.

6.1. Stellar mass function

The stellar mass function—the distribution function of galaxies by stellar mass—is one of the most essential metrics for comparing galaxy populations (e.g., Weaver et al. 2023). The stellar mass function depends on physical processes ranging over a variety of scales, from cloud-scale gas cooling and star formation to large-scale galaxy interactions and tidal torques. ML methods that aim to paint galaxy properties onto subhalos should be able to reconstruct the stellar mass (or luminosity) function accurately.

In Figure 5, we show the stellar mass function, ϕ , from EBM-base (solid yellow), EBM-DisPerSE (dotted green), EBM-overdensity (dashed blue), and GNN (solid purple) predictions. We show the TNG300 ground truth stellar mass function in thick solid gray. All the ML models predict accurate stellar mass functions in the range $9.5 < \log(M_*/M_\odot) < 12$, demonstrating their general success at estimating galaxy stellar mass at the population level. While the EBM models begin to falter above $\log(M_*/M_\odot) \approx 12.25$, the GNN continues to recover the stellar mass function up to $\log(M_*/M_\odot) \approx 12.6$. These underpredictions reflect the well-known limitation of ML models to capture the extrema of the target distribution, where the training data offer very few examples. Indeed, the most massive galaxies are only found at the centers of rare, massive galaxy clusters (and tend

to have very extended and diffuse stellar mass distributions; e.g., Pillepich et al. 2018, making their properties difficult to model). For these extreme examples, it is often expected that any statistical model performance will suffer or break down (signifying a physical shift in algorithmically learned scaling relations; e.g., Wu 2020).⁵ However, we confirm that the EBM and GNN models can accurately reproduce the stellar mass function for common, well-represented galaxies.

6.2. Two-point correlation function

Methods that use (small-scale) environment information can affect downstream clustering analyses, which in turn can introduce biases in cosmological applications. We test whether our EBM or GNN approach corrupts the galaxy clustering information by measuring galaxy-galaxy correlation functions, $\xi(r)$, using the `treecorr` code. The count-count correlations are measured in logarithmically spaced radial bins from 0.5 and 20 Mpc.⁶ We split galaxies into two stellar mass samples, $9 \leq \log(M_*/M_\odot) < 10.5$ and $\log(M_*/M_\odot) \geq 10.5$, where M_* is independently predicted using each ML model, optimized using the full training sample. We normalize two-point correlation functions by the ground truth two-point correlation function, $\xi^{\text{TNG300}}(r)$, based on the TNG300 fully hydrodynamic simulation. We estimate uncertainties using shot noise variance and the covariance derived from marked bootstrap resampling (see Loh 2008). We also report two metrics: first, we compute the weighted mean ratio of $\xi^{\text{Model}}(r)/\xi^{\text{TNG300}}(r)$, which measures the level of bias in modeled correlation function. Second, we compute the coefficient of determination, r^2 , between each $\xi^{\text{Model}}(r)$ and $\xi^{\text{TNG300}}(r)$, which measures how well the two correlation functions agree. Our results are shown in Figure 6.

We find that all ML models generally reproduce the correct two-point correlation function, especially for large separations, which should not be surprising given that these scales are in the linear regime. The models that leverage environmental features perform as well or better than the EBM-base model. For separations smaller than a few Mpc, and for higher-mass galaxies, the errors on model-predicted correlation functions range up to ~ 0.1 dex (panel (b) of Figure 6). At $r \gtrsim 1$ Mpc, the EBM-base and EBM-DisPerSE models cluster lower-mass galaxies too strongly, and higher-

⁵ In fact, if ML models do *not* break down at the extrema, then this could indicate a surprising continuation of scaling laws into extremal regimes even when new physical processes might become important (e.g., Holwerda et al. 2021).

⁶ At scales > 20 Mpc, all models can almost perfectly recover the TNG300 two-point correlation function.

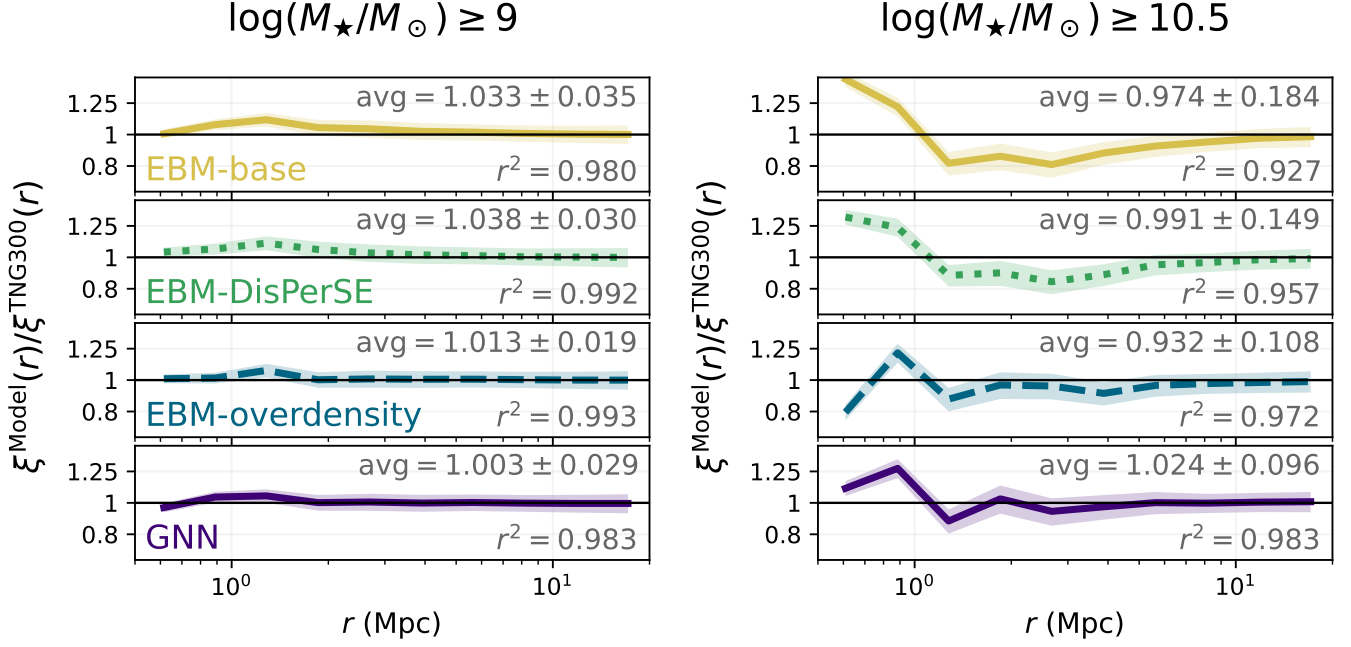


Figure 6. Comparing different models’ two-point correlation functions. The galaxy-galaxy correlation function $\xi^{\text{Model}}(r)$ from EBM and GNN models, normalized by the “true” TNG300 correlation function $\xi^{\text{TNG300}}(r)$, for low-mass (*left*) and high-mass (*right*) bins. We also display the weighted average $\xi^{\text{Model}}(r)/\xi^{\text{TNG300}}(r)$ and the coefficient of determination, r^2 .

mass galaxies too weakly. The EBM-overdensity and GNN models are less prone to these small biases and give robust results. The GNN appears to perform the best in terms of the mean ratio of correlation functions and ρ , although there is still some scatter in the higher-mass bin. Ultimately, the two-point correlation function does not appear to be highly sensitive to differences between our model predictions. We conclude that our methods do not introduce strong biases in the correlation statistics and that a GNN overall performs best.

6.3. SHMR dependence on overdensity

We also investigate how the modeled SHMR varies with environment. Our results and interpretation in Section 5.3 showed that large-scale surroundings on 3 Mpc scales are particularly influential for the SHMR, so we parameterize the environment using $\delta_3 \text{ Mpc}$. In Figure 7, we compare the stellar-to-halo mass ratio, $\log(M_*/M_{\text{halo}})$ against $\delta_3 \text{ Mpc}$ for both central (*upper*) and satellite (*lower*) subhalos. We plot this relationship for a simple M_{halo} SHAM model (*left-most* panel), EBM models (*middle* panels), and the GNN (*right-most* panel). The ground truth TNG300 simulation is shown in all panels as gray contours.

We see a strong “ridge line” in $\log(M_*/M_{\text{halo}})$ versus $\delta_3 \text{ Mpc}$ in central halos for some models (*upper* panels in Figure 7). The ridge is inhabited by lonely central halos with no other subhalos within 3 Mpc, such that the overdensity is equal to the central halo mass. The

monotonic SHMR from abundance matching leads to a particularly tight ridge line (left-most panel). The GNN model is vastly better than EBM models at softening this ridge line. However, we note that the ridge is not a complete artifact, and manifests as a broad trend even in the TNG300 version of the $\log(M_*/M_{\text{halo}})$ versus $\delta_3 \text{ Mpc}$ relationship for centrals. We conclude that the GNN most realistically recovers this probe of the galaxy–halo–environment connection.

6.4. Variations in the optimal GNN linking length

A halo’s assembly history is correlated with its mass and depends on whether it is a central or satellite. We expect this to manifest as systematic variations in the optimal environmental length scale. To test this, we bin the model predictions by subhalo mass, i.e. $\log(M_{\text{halo}}/M_\odot) < 12$ and ≥ 12 . A halo mass of $10^{12} M_\odot$ is near the characteristic mass that creates a break in the SHMR (see, e.g., Moster et al. 2010; Engler et al. 2021). These results are shown in Figure 8. Note that we do not retrain the models, but simply split the validation results into low- and high-mass subsamples. We also observe that the typical errors associated with stellar mass predictions in the two mass bins are different, ranging from $\gtrsim 0.17$ in the lower-mass bin to $\gtrsim 0.12$ in the higher-mass bin. The EBM-overdensity model is also less sensitive to linking length in the higher-mass bin. Although we find qualitatively similar results to before, the optimal values of L vary mod-

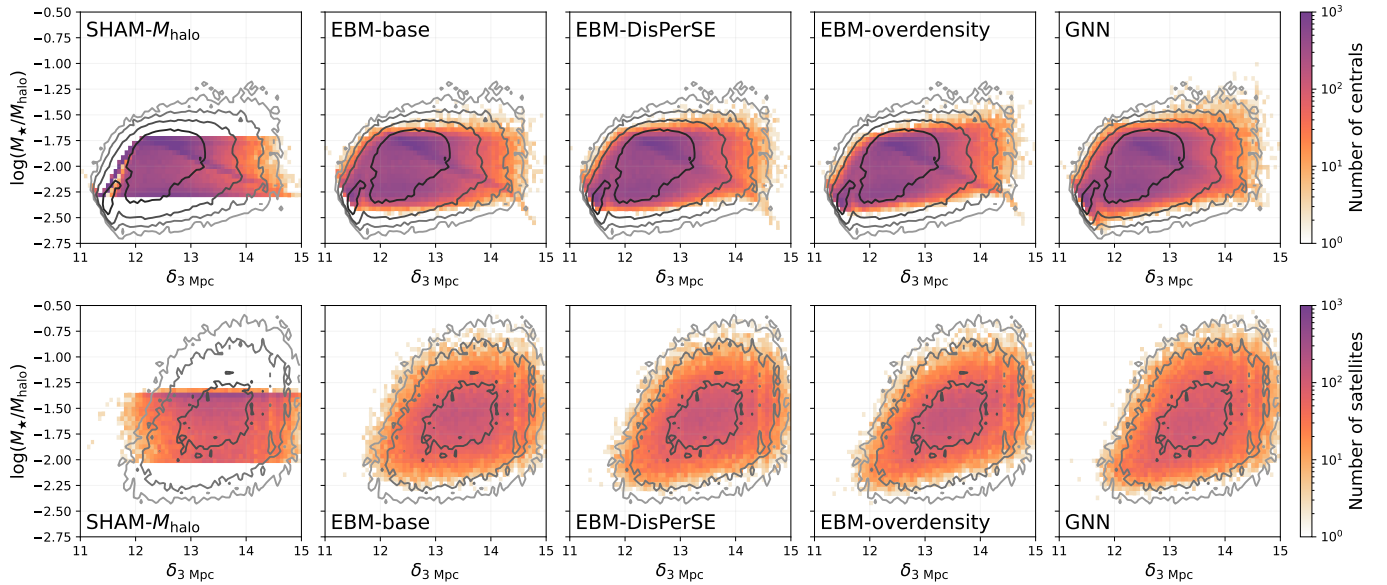


Figure 7. In a comparison of M_*/M_{halo} against overdensity, the GNN is most similar to TNG300 (contours). We show the stellar-to-halo mass ratio against average overdensity on 3 Mpc scales, for centrals (*upper*) and satellites (*lower*). The gray contours show the same comparison for TNG300 with levels at 4, 16, 64, 256. All panels are shown on the same scales.

estly with subhalo mass. For EBM-overdensity, these are 3 Mpc for $\log(M_{\text{halo}}/M_{\odot}) < 12$, and 3.5 Mpc for $\log(M_{\text{halo}}/M_{\odot}) \geq 12$. The GNN exhibits more steeply declining errors at large L for the higher-mass bin, indicating that it can better leverage large-scale environmental information surrounding more massive subhalos.

We also split the model prediction results by whether each subhalo is a satellite or central, shown respectively in left and right panels of Figure 9. We again find that the typical RMSE losses are different, and that they strongly vary with L . Satellites appear to leverage information on smaller scales (~ 2.5 Mpc) while centrals exploit information on larger scales (~ 3.5 Mpc); this difference is particularly apparent from the EBM-overdensity results. We can also draw similar conclusions from the GNN results, which are largely flat for $L > 3$ Mpc for satellites, in contrast to centrals which show continued improvement beyond $L > 3$ Mpc. Our results demonstrate that the optimal L systematically varies with a galaxy’s halo mass and whether it is a central.

6.5. Connection to galactic conformity?

We have found that the connection between subhalos and galaxies depends critically on their surroundings on ~ 3 Mpc distance scales.⁷ This length scale is similar to galactic conformity correlation scales (beyond the central halo’s virial radius, i.e., two-halo conformity). One

explanation for galactic conformity is that “pre-heating” from star formation or active galactic nuclei heats gas and inhibits future star formation, even if that gas is accreted into surrounding systems at later times (e.g., Kauffmann et al. 2013). Hearin et al. (2016) posit that large-scale tidal forces are responsible for synchronizing halo accretion rates over several Mpc. Other works find that gas reservoirs in both central and satellite galaxies can be stripped as they collectively enter through filaments or the outskirts of the most massive cluster-scale halos, which correlates their mass accretion and star formation histories (e.g., Bahé et al. 2013; Zinger et al. 2018; Ayromlou et al. 2023). Alternatively, Zu & Mandelbaum (2018) contend that a simple halo quenching model, with no assembly bias or direct environmental processes, can fully reproduce the observed galactic conformity clustering signal.

Our study probes large-scale environment at a single simulation snapshot, and does not include any direct parameterization of assembly bias. For example, we do not use peak halo mass or subhalo mass at time of accretion (e.g., Nagai & Kravtsov 2005; Conroy et al. 2006), so our work only considers the galaxy–halo connection through the lens of large-scale environment. Indeed, our results and interpretation in Section 5 demonstrate that environmental impacts can be captured without explicitly accounting for assembly bias (although accounting for the halo merger history can further assist with stellar mass predictions; see, e.g., Jespersen et al. 2022). However, we emphasize that these findings do not directly explain galactic conformity or its origin.

⁷ Nonetheless, the EBM-overdensity and GNN models can exploit environmental information on scales larger than 3 Mpc.

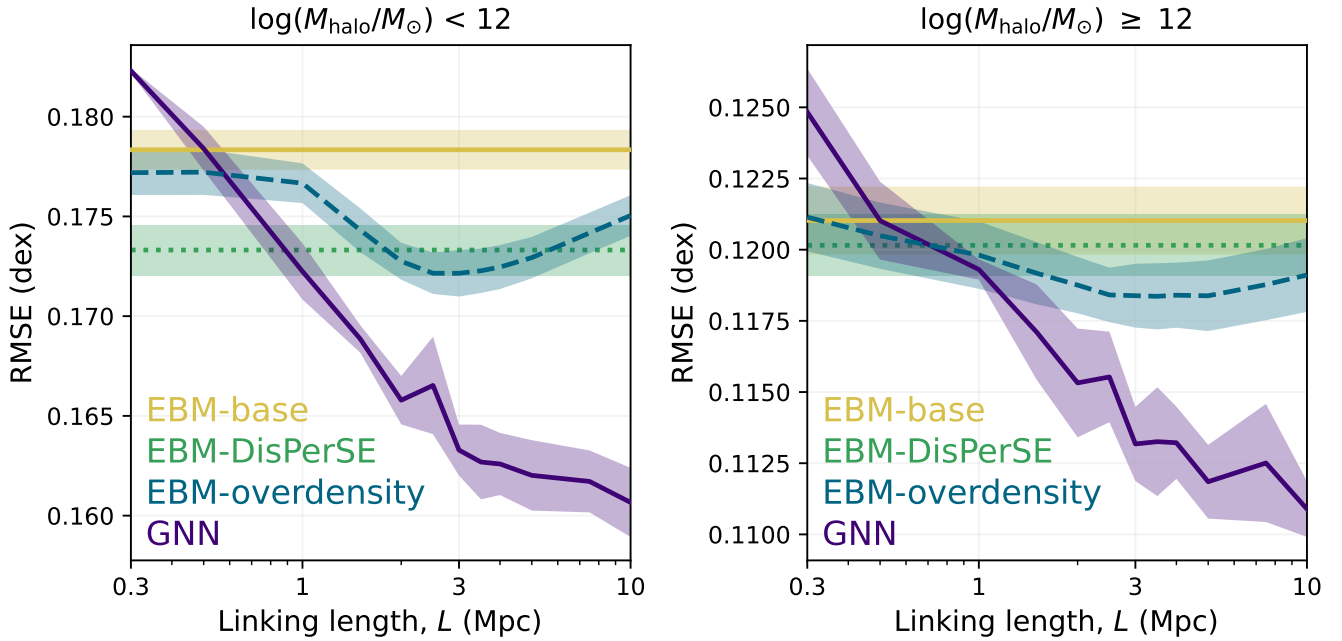


Figure 8. The **EBM-overdensity** and **GNN** models demonstrate improved performance at larger L for higher-mass subhalos. We show how different models perform as a function of L for lower-mass (*left*) and higher-mass (*right*) subhalos. Note that the y axes show different scales.

6.6. The inductive biases of graph-based models

Graphs are natural representations of cosmic structure, i.e., they capture the inductive biases of our problem. There is no canonical ordering for a subhalo catalog, which is reflected in the permutation equivariance of graphs. Interactions between galaxies and their surroundings are also local, which can also be enforced via graph connectivity on linking distance scales, L . Additionally, graphs impose a relational structure between entities that are not reflected in other ML models, e.g., tabular models or fully connected neural networks (Kamdar et al. 2016; Agarwal et al. 2018; Calderon & Berlind 2019; Necib et al. 2020; Wadekar et al. 2020; Moster et al. 2021; Delgado et al. 2022; Bowden et al. 2023; Hausen et al. 2023). Our subhalo catalogs are actually point clouds in a $3d$ position space,⁸ and we enforce these geometric constraints by making our graph models invariant under rotations, translations, and reflections (i.e., the $\mathbb{E}(3)$ group action). Convolutional neural networks (CNNs) can also map baryons onto dark matter halos (Zhang et al. 2019; Kasmanoff et al. 2020; Mohammad et al. 2022), and incorporate local relationships, but they make other assumptions about the geometric structure of the data, e.g., CNNs represent mat-

ter distributions on a coarse-grained grid. Given the nature of our data, we strongly recommend using graphs or point clouds to model galaxy large-scale structure.

6.7. Caveats

Here we mention several caveats about our methodology and analysis. First, we have only investigated the environmental length scales in TNG300, and not for other TNG box sizes or different simulation codes. In particular, other simulations impose different physical models and subgrid prescriptions, which can cause differences in the galaxy–halo–environment connection. Even for TNG300, we note that the optimal distance scale may change depending on the subhalo catalog selection criteria (see, e.g., Section 6.4). Different physics models or selection effects can lead to different “optimal” length scales.

We also note that our use of DisPerSE distance features is limited to a single TNG300 value-added catalog (Duckworth et al. 2019). This catalog is not meant to exhaustively cover all parameterizations of cosmic web features. It is also known that the DisPerSE algorithm can be tuned via several hyperparameters (such as the persistence threshold; Sousbie 2011), and that these hyperparameter choices may impact the importance of EBM-DisPerSE model features. Other studies have also run DisPerSE on TNG300 with differ-

⁸ Point clouds have a notion of position, and therefore obey geometric inductive biases.

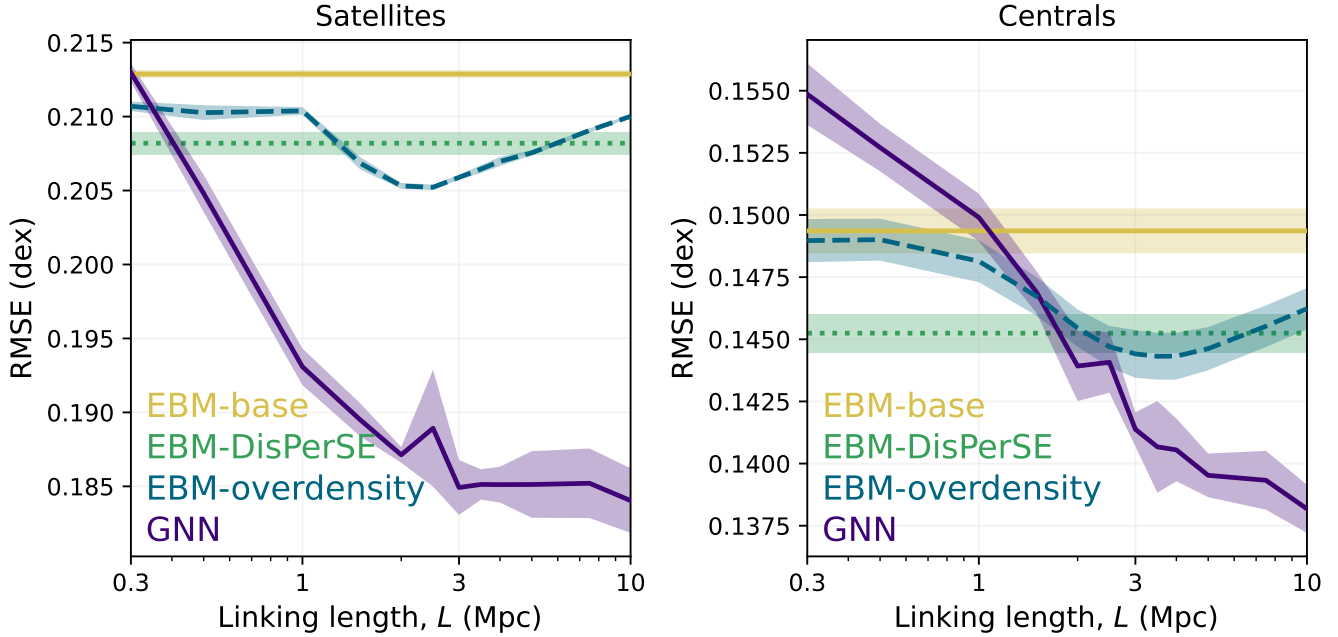


Figure 9. The **EBM-overdensity** and **GNN** models exhibit better performance at larger L for centrals. We show how different models perform as a function of L for centrals (*left*) and satellites (*right*). Note that the y axes show different scales.

ent hyperparameter choices (e.g., a different persistence threshold; Galárraga-Espinosa et al. 2020, 2022).

The final caveat stems from our subhalo catalog, which is crossmatched between the dark matter only and hydrodynamic simulations of TNG300 runs. We have used only the most robust subhalos found with SUBFIND and matched to dark matter only runs using both LHalotree and SubLink, but the resulting subhalo population may still be biased or have incorrect properties (see, e.g., Green et al. 2021; Benson & Du 2022; Mansfield et al. 2023). On top of this, there is a “butterfly effect” in numerical simulations that can contribute significant scatter to individual galaxy-to-halo mass ratios (Genel et al. 2019). We do not attempt to correct for these issues, as they go beyond the scope of our aim to understand galaxy environmental length scales. See Chuang et al. (2023) for a further discussion of the impact of the butterfly effect on ML studies using simulations. Our work is an initial foray toward understanding environmental length scales via explainable ML models and GNNs; additional studies are needed to confirm that these results generalize to other data sets.

7. CONCLUSIONS

In this work, we investigate which distance scales and environmental measures best characterize the galaxy–halo–environment connection in the Illustris TNG300 simulation. We learn to predict the stellar mass from

dark matter halo properties using interpretable machine learning models (Explainable Boosting Machines; EBMs) and graph neural networks (GNNs; see Figure 1 for a schematic diagram). Our analysis compares an EBM-base model, an EBM-DisPerSE model with cosmic web distance features, an EBM-overdensity model with spherically averaged overdensity features on length scale L ranging between 0.3 through 10 Mpc, and a GNN with subhalos connected on those same length scales. We evaluate each model using the root mean squared error (RSME) of stellar mass predictions compared to the hydrodynamic simulation, where the latter is treated as the ground truth. Our code is publically available on Github at <https://github.com/jwuphysics/halo-gnns/tree/linking-length>.

Our main conclusions are as follows:

1. An EBM model performs best if provided spherically averaged overdensity on 3 Mpc scales (Figure 2).
2. We interpret the EBM using SHapley Additive Explanations (SHAP), and find that the overdensity features most important for describing the galaxy–halo connection are those on scales up to ~ 3 Mpc (Figure 4). At larger distances, overdensity is less informative but still contributes new information.
3. If we train a model that includes the 3 Mpc overdensity feature as well as cosmic web features,

then the simple overdensity feature is considerably more important than all cosmic web features (Figure 3).

4. Our GNN outperforms all other models by simply linking galaxies together on large scales (Figure 2).
5. The GNN performance continues to improve at $L \gtrsim 3$ Mpc, albeit at a slower pace, indicating that the GNN learns valuable large-scale features. These very large-scale environmental features are preferentially useful for modeling the galaxy–halo connection at high mass and for central halos (Figures 8 and 9, respectively).

We ensure that our ML algorithms recover accurate stellar masses functions and two-point correlation functions (Figures 5 and 6, respectively). We also compare the stellar-to-halo mass ratio, $\log(M_*/M_{\text{halo}})$, against spherically averaged overdensity, $\delta_{3 \text{ Mpc}}$, which shows that the GNN most realistically accounts for the interplay between the SHMR and environmental overdensity (Figure 7).

This work is an initial exploration of the environmental distance scales that influence the galaxy–halo relation in a specific model of galaxy formation and is not without its caveats and limitations (see, e.g., Section 6.7). However, we demonstrate that interpretable EBM models are capable of divulging important information about complex physical interactions. An $\mathbb{E}(3)$ -invariant GNN can outperform these EBM models simply by learning the galaxy–halo–environment connection from data; we do not need to explicitly provide the GNN any environmental features. We believe that GNNs, with their relational inductive biases and group-invariant/equivariant constraints, will continue to lead

the charge in efficient, interpretable ML for the physical sciences. Follow-up studies with symbolic regression (e.g., PySR; Cranmer 2023) or other SHAP capabilities (e.g., kernel explanations; Lundberg & Lee 2017) can add another layer of interpretability to the work presented here. For understanding the features characterizing the galaxy–halo connection in the real universe, it will be important to expand this work beyond the single simulation considered herein to understand how generic these findings are for other models.

Software: `astropy` (Astropy Collaboration et al. 2022), `InterpretML` (Nori et al. 2019), `matplotlib` (Hunter 2007), `NumPy` (Harris et al. 2020), `PyTorch` (Paszke et al. 2019), `pytorch-geometric` (Fey & Lenssen 2019), `SciPy` (Virtanen et al. 2020), `shap` (Lundberg & Lee 2017), `statsmodels` (Seabold & Perktold 2010), `treecorr` (Jarvis et al. 2004)

- 1 The authors are grateful to Peter Behroozi, Haley
- 2 Bowden, Suchetha Cooray, Daniela Galarraga-Espinosa,
- 3 Martin Rey, Tjitske Starkenburg, and Paco Villaescusa-
- 4 Navarro, who provided valuable discussions. We also
- 5 thank the Kavli Institute for Theoretical Physics “Build-
- 6 ing a Physical Understanding of Galaxy Evolution with
- 7 Data-driven Astronomy” program, where this work be-
- 8 gan. This research was supported in part by the
- 9 National Science Foundation under Grant No. NSF
- 10 PHY-1748958. This work used Rockfish - GPU re-
- 11 sources at Johns Hopkins University through allocation
- 12 PHY230101 from the Advanced Cyberinfrastructure Co-
- 13 ordination Ecosystem: Services & Support (ACCESS)
- 14 program, which is supported by National Science Foun-
- 15 dation grants NSF PHY-2138259, PHY-2138286, PHY-
- 16 2138307, PHY-2137603, and PHY-2138296.

APPENDIX

A. GNN DETAILS

A.1. Data preprocessing

Model training is often easier if the inputs resemble (or are close to) Gaussian distributions. We normalize all subhalo velocities by 100 km s^{-1} , and logarithmically scale the subhalo properties M_{halo} , V_{max} , and M_* . We also rescale the DisPerSE cosmic web parameters so that they have zero mean and unit variance. In order to ensure translational invariance, we also recenter all subhalo positions to the center of mass of the subhalos.

A.2. GNN architecture details

In Section 3.2.2, we described the GNN architecture, which is composed of $N_{\text{unshared}} = 8$ unique versions of the edge MLP $\phi^{(\ell)}$, and a node MLP ψ that comprises three parts, ψ_1 , ψ_2 , and ψ_3 . The network ψ_1 ingests concatenated outputs of the edge MLPs, and ψ_2 ingests the node features; ψ_3 ingests the outputs of ψ_1 and ψ_2 and returns the final prediction. Panel (c) of Figure 1 also provides a high-level graphic of the GNN layers. We use $N_{\text{hidden}} = 64$ and $N_{\text{latent}} = 16$. The total parameter count is 89,650: 50,304 for all $\{\phi^{(\ell)}\}_{(\ell)}$, 26,976 for ψ_1 , 5,712 for ψ_2 , and 6,658 for ψ_3 . In Table 2, we list the

layer names, parameter counts, input sizes, and output sizes for all neural network layers in our GNN.

We also tested an architecture variant with a single MLP ψ that takes in all $3 \times N_{\text{unshared}} \times N_{\text{latent}} = 768$ pooled edge features alongside the two node features, and directly makes predictions. However, there are many more pooled edge features than node features, which makes it difficult for the network to learn a robust combination in a single MLP. We found that the GNN performance improves when we train ψ_1 to distill the 768 (highly correlated) edge features into 16 features using ψ_1 .

A.3. GNN optimization hyperparameters

We performed a basic hyperparameter search over several variables. The results are summarized below, along with more general remarks about GNN and neural network optimization. In particular, the first two choices—removing loops and using the `ClusterLoader` sampler—dramatically improved our GNN performance.

Remove (self-)loops from graph. Loops on graphs, i.e., edges that connect a node to itself, have a negative effect on performance. This is likely because loops interfere with edge features $d_{ii}^{(x)} = 0$, which in turn makes it difficult for the model to learn a $1/d^n$ power law that describes gravity, tides, or other local interactions.

Sample large batches of clustered nodes beyond the linking length. We found that the Pytorch-Geometric `ClusterLoader` sampling strategy (Chiang et al. 2019) outperforms random node sampling or simple neighborhood-based sampling. The `ClusterLoader` method uses graph clustering to identify relatively dense subgraphs and batch them together, resulting in efficient training and significantly lower loss. We note that, while

the `ClusterLoader` algorithm performs well for large and well-connected graphs, it seems to perform poorly at very small linking lengths (i.e. at $L \approx 0.3$ Mpc the GNN performs worse than the EBM models; Figure 2). We speculate that the `ClusterLoader` sampling strategy fails in the case of very sparse graphs, resulting in inefficient training.

Adaptive optimization. We use the Adam optimizer with decoupled weight decay (AdamW; Kingma & Ba 2014; Loshchilov & Hutter 2019). We set the (β_1, β_2) momentum parameters to $(0.9, 0.95)$.

Learning rate = 10^{-2} . The learning rate determines the size of the model parameter updates. This important hyperparameter also covaries with many other hyperparameters. Because we are using a relatively small neural network, we found that the learning rate can be made fairly large (i.e., relative to the values of $\sim 10^{-4} - 10^{-5}$ often used for training deeper neural networks).

Weight decay = 10^{-4} . Weight decay is analogous to L2 regularization when using the AdamW optimizer. We found that weight decay lowers the gap between training and validation loss.

Learning rate schedule. Although we begin training at a relatively high learning rate (0.01), we reduce the learning rate to 0.002 at epoch 75, 0.0004 at epoch 150, and 0.00008 at epoch 225. This annealing process helps stabilize the optimization procedure and achieve a lower loss.

Noise augmentation. We add random noise to the node and edge features of the GNN to help it learn representations that are robust to noise (e.g., Murphy et al. 2019; Godwin et al. 2022). During training, we sample and add Gaussian-distributed, zero-mean noise scaled to 0.0003 times each input feature’s scatter.

REFERENCES

- Agarwal, S., Davé, R., & Bassett, B. A. 2018, MNRAS, 478, 3410, doi: [10.1093/mnras/sty1169](https://doi.org/10.1093/mnras/sty1169)
- Astropy Collaboration, Price-Whelan, A. M., Lim, P. L., et al. 2022, ApJ, 935, 167, doi: [10.3847/1538-4357/ac7c74](https://doi.org/10.3847/1538-4357/ac7c74)
- Ayroulou, M., Kauffmann, G., Anand, A., & White, S. D. M. 2023, MNRAS, 519, 1913, doi: [10.1093/mnras/stac3637](https://doi.org/10.1093/mnras/stac3637)
- Bahé, Y. M., McCarthy, I. G., Balogh, M. L., & Font, A. S. 2013, MNRAS, 430, 3017, doi: [10.1093/mnras/stt109](https://doi.org/10.1093/mnras/stt109)
- Battaglia, P. W., Hamrick, J. B., Bapst, V., et al. 2018, arXiv e-prints, arXiv:1806.01261, doi: [10.48550/arXiv.1806.01261](https://doi.org/10.48550/arXiv.1806.01261)
- Benson, A. J., Cole, S., Frenk, C. S., Baugh, C. M., & Lacey, C. G. 2000, MNRAS, 311, 793, doi: [10.1046/j.1365-8711.2000.03101.x](https://doi.org/10.1046/j.1365-8711.2000.03101.x)
- Benson, A. J., & Du, X. 2022, MNRAS, 517, 1398, doi: [10.1093/mnras/stac2750](https://doi.org/10.1093/mnras/stac2750)
- Berlind, A. A., & Weinberg, D. H. 2002, ApJ, 575, 587, doi: [10.1086/341469](https://doi.org/10.1086/341469)
- Blanton, M. R., Eisenstein, D., Hogg, D. W., Schlegel, D. J., & Brinkmann, J. 2005, ApJ, 629, 143, doi: [10.1086/422897](https://doi.org/10.1086/422897)
- Blanton, M. R., Eisenstein, D., Hogg, D. W., & Zehavi, I. 2006, ApJ, 645, 977, doi: [10.1086/500918](https://doi.org/10.1086/500918)

Table 2. Details for all MLPs in the GNN. The total parameter counts are given for each MLP, as well as the breakdown for each individual layer. The full model includes $N_{\text{unshared}} = 8$ versions of $\phi^{(\ell)}$. The total parameter count is 89,650.

Layer	Number of parameters	Input size	Output size
$\phi^{(\ell)}$ (Edge MLP)	Total: 6,288	12	16
Linear1	832	12	64
LayerNorm1	128	64	64
SiLU1	—	64	64
Linear2	4,160	64	64
LayerNorm2	128	64	64
SiLU2	—	64	64
Linear3	1,040	64	16
ψ_1 (Node MLP 1)	Total: 26,976	384	16
Linear1	24,640	384	64
LayerNorm1	128	64	64
SiLU1	—	64	64
Linear2	1,040	64	64
LayerNorm2	128	64	64
SiLU2	—	64	64
Linear3	1,040	64	16
ψ_2 (Node MLP 2)	Total: 5,712	3	16
Linear1	256	3	64
LayerNorm1	128	64	64
SiLU1	—	64	64
Linear2	4,160	64	64
LayerNorm2	128	64	64
SiLU2	—	64	64
Linear3	1,040	64	16
ψ_3 (Node MLP 3)	Total: 6,658	32	2
Linear1	2,112	32	64
LayerNorm1	128	64	64
SiLU1	—	64	64
Linear2	4,160	64	64
LayerNorm2	128	64	64
SiLU2	—	64	64
Linear3	130	64	2

Bonjean, V., Aghanim, N., Douspis, M., Malavasi, N., & Tanimura, H. 2020, *A&A*, 638, A75,
doi: [10.1051/0004-6361/201937313](https://doi.org/10.1051/0004-6361/201937313)

Bowden, H., Behroozi, P., & Hearin, A. 2023, *The Open Journal of Astrophysics*, 6, 37,
doi: [10.21105/astro.2307.07549](https://doi.org/10.21105/astro.2307.07549)

Breiman, L. 2001, *Machine Learning*, 45, 5,
doi: [10.1023/A:1010933404324](https://doi.org/10.1023/A:1010933404324)

Bronstein, M. M., Bruna, J., Cohen, T., & Veličković, P. 2021, arXiv e-prints, arXiv:2104.13478,
doi: [10.48550/arXiv.2104.13478](https://doi.org/10.48550/arXiv.2104.13478)

Bullock, J. S., & Boylan-Kolchin, M. 2017, *ARA&A*, 55, 343, doi: [10.1146/annurev-astro-091916-055313](https://doi.org/10.1146/annurev-astro-091916-055313)

Calderon, V. F., & Berlind, A. A. 2019, *MNRAS*, 490, 2367, doi: [10.1093/mnras/stz2775](https://doi.org/10.1093/mnras/stz2775)

- Chiang, W.-L., Liu, X., Si, S., et al. 2019, in Proceedings of the 25th ACM SIGKDD International Conference on Knowledge Discovery & Data Mining (ACM), doi: [10.1145/3292500.3330925](https://doi.org/10.1145/3292500.3330925)
- Christensen, C. R., Brooks, A., Munshi, F., et al. 2023, arXiv e-prints, arXiv:2311.04975, doi: [10.48550/arXiv.2311.04975](https://doi.org/10.48550/arXiv.2311.04975)
- Chuang, C.-Y., Kragh Jespersen, C., Lin, Y.-T., Ho, S., & Genel, S. 2023, arXiv e-prints, arXiv:2311.09162, doi: [10.48550/arXiv.2311.09162](https://doi.org/10.48550/arXiv.2311.09162)
- Chuang, C.-Y., & Lin, Y.-T. 2023, ApJ, 944, 207, doi: [10.3847/1538-4357/acb5f3](https://doi.org/10.3847/1538-4357/acb5f3)
- Conroy, C., Wechsler, R. H., & Kravtsov, A. V. 2006, ApJ, 647, 201, doi: [10.1086/503602](https://doi.org/10.1086/503602)
- Cranmer, M. 2023, Interpretable Machine Learning for Science with PySR and SymbolicRegression.jl, arXiv, doi: [10.48550/arXiv.2305.01582](https://doi.org/10.48550/arXiv.2305.01582)
- Delgado, A. M., Wadekar, D., Hadzhiyska, B., et al. 2022, MNRAS, 515, 2733, doi: [10.1093/mnras/stac1951](https://doi.org/10.1093/mnras/stac1951)
- Dressler, A. 1980, ApJ, 236, 351, doi: [10.1086/157753](https://doi.org/10.1086/157753)
- Duckworth, C., Tojeiro, R., & Kraljic, K. 2020, MNRAS, 492, 1869, doi: [10.1093/mnras/stz3575](https://doi.org/10.1093/mnras/stz3575)
- Duckworth, C., Tojeiro, R., Kraljic, K., et al. 2019, MNRAS, 483, 172, doi: [10.1093/mnras/sty3101](https://doi.org/10.1093/mnras/sty3101)
- Engler, C., Pillepich, A., Joshi, G. D., et al. 2021, MNRAS, 500, 3957, doi: [10.1093/mnras/staa3505](https://doi.org/10.1093/mnras/staa3505)
- Fey, M., & Lenssen, J. E. 2019, Fast Graph Representation Learning with PyTorch Geometric. https://github.com/pyg-team/pytorch_geometric
- Friedman, J. H. 2001, The Annals of Statistics, 29, 1189, doi: [10.1214/aos/1013203451](https://doi.org/10.1214/aos/1013203451)
- Galárraga-Espinosa, D., Aghanim, N., Langer, M., Gouin, C., & Malavasi, N. 2020, A&A, 641, A173, doi: [10.1051/0004-6361/202037986](https://doi.org/10.1051/0004-6361/202037986)
- Galárraga-Espinosa, D., Langer, M., & Aghanim, N. 2022, A&A, 661, A115, doi: [10.1051/0004-6361/202141974](https://doi.org/10.1051/0004-6361/202141974)
- Geiger, M., & Smidt, T. 2022, arXiv e-prints, arXiv:2207.09453, doi: [10.48550/arXiv.2207.09453](https://doi.org/10.48550/arXiv.2207.09453)
- Genel, S., Bryan, G. L., Springel, V., et al. 2019, ApJ, 871, 21, doi: [10.3847/1538-4357/aaf4bb](https://doi.org/10.3847/1538-4357/aaf4bb)
- Godwin, J., Schaarschmidt, M., Gaunt, A. L., et al. 2022, in International Conference on Learning Representations. <https://openreview.net/forum?id=1wVvweK3oIb>
- Green, S. B., van den Bosch, F. C., & Jiang, F. 2021, MNRAS, 503, 4075, doi: [10.1093/mnras/stab696](https://doi.org/10.1093/mnras/stab696)
- Hahn, O., Porciani, C., Dekel, A., & Carollo, C. M. 2009, MNRAS, 398, 1742, doi: [10.1111/j.1365-2966.2009.15271.x](https://doi.org/10.1111/j.1365-2966.2009.15271.x)
- Harris, C. R., Millman, K. J., van der Walt, S. J., et al. 2020, Nature, 585, 357, doi: [10.1038/s41586-020-2649-2](https://doi.org/10.1038/s41586-020-2649-2)
- Hasan, F., Burchett, J. N., Hellinger, D., et al. 2023, Filaments of The Slime Mold Cosmic Web And How They Affect Galaxy Evolution. <https://arxiv.org/abs/2311.01443>
- Hastie, T., & Tibshirani, R. 1986, Statistical Science, 1, 297, doi: [10.1214/ss/1177013604](https://doi.org/10.1214/ss/1177013604)
- Hausen, R., Robertson, B. E., Zhu, H., et al. 2023, ApJ, 945, 122, doi: [10.3847/1538-4357/acb25c](https://doi.org/10.3847/1538-4357/acb25c)
- Hearin, A. P., Behroozi, P. S., & van den Bosch, F. C. 2016, MNRAS, 461, 2135, doi: [10.1093/mnras/stw1462](https://doi.org/10.1093/mnras/stw1462)
- Hearin, A. P., Watson, D. F., & van den Bosch, F. C. 2015, MNRAS, 452, 1958, doi: [10.1093/mnras/stv1358](https://doi.org/10.1093/mnras/stv1358)
- Hogg, D. W., Blanton, M. R., Eisenstein, D. J., et al. 2003, ApJL, 585, L5, doi: [10.1086/374238](https://doi.org/10.1086/374238)
- Holwerda, B. W., Wu, J. F., Keel, W. C., et al. 2021, ApJ, 914, 142, doi: [10.3847/1538-4357/abffcc](https://doi.org/10.3847/1538-4357/abffcc)
- Hoosain, M., Blyth, S.-L., Skelton, R. E., et al. 2024, MNRAS, doi: [10.1093/mnras/stae174](https://doi.org/10.1093/mnras/stae174)
- Hunter, J. D. 2007, Computing in Science & Engineering, 9, 90, doi: [10.1109/MCSE.2007.55](https://doi.org/10.1109/MCSE.2007.55)
- Huppenkothen, D., Ntampaka, M., Ho, M., et al. 2023, arXiv e-prints, arXiv:2310.12528, doi: [10.48550/arXiv.2310.12528](https://doi.org/10.48550/arXiv.2310.12528)
- Iyer, K. G., Tacchella, S., Genel, S., et al. 2020, MNRAS, 498, 430, doi: [10.1093/mnras/staa2150](https://doi.org/10.1093/mnras/staa2150)
- Jarvis, M., Bernstein, G., & Jain, B. 2004, MNRAS, 352, 338, doi: [10.1111/j.1365-2966.2004.07926.x](https://doi.org/10.1111/j.1365-2966.2004.07926.x)
- Jespersen, C. K., Cranmer, M., Melchior, P., et al. 2022, ApJ, 941, 7, doi: [10.3847/1538-4357/ac9b18](https://doi.org/10.3847/1538-4357/ac9b18)
- Kamdar, H. M., Turk, M. J., & Brunner, R. J. 2016, MNRAS, 457, 1162, doi: [10.1093/mnras/stv2981](https://doi.org/10.1093/mnras/stv2981)
- Kasmanoff, N., Villaescusa-Navarro, F., Tinker, J., & Ho, S. 2020, arXiv e-prints, arXiv:2012.00186, doi: [10.48550/arXiv.2012.00186](https://doi.org/10.48550/arXiv.2012.00186)
- Kauffmann, G., Li, C., Zhang, W., & Weinmann, S. 2013, MNRAS, 430, 1447, doi: [10.1093/mnras/stt007](https://doi.org/10.1093/mnras/stt007)
- Kauffmann, G., White, S. D. M., Heckman, T. M., et al. 2004, MNRAS, 353, 713, doi: [10.1111/j.1365-2966.2004.08117.x](https://doi.org/10.1111/j.1365-2966.2004.08117.x)
- Kingma, D. P., & Ba, J. 2014, arXiv preprint arXiv:1412.6980
- Kravtsov, A. V., Berlind, A. A., Wechsler, R. H., et al. 2004, ApJ, 609, 35, doi: [10.1086/420959](https://doi.org/10.1086/420959)
- Lacerna, I., Contreras, S., González, R. E., Padilla, N., & Gonzalez-Perez, V. 2018, MNRAS, 475, 1177, doi: [10.1093/mnras/stx3253](https://doi.org/10.1093/mnras/stx3253)
- Lacerna, I., Rodriguez, F., Montero-Dorta, A. D., et al. 2022, MNRAS, 513, 2271, doi: [10.1093/mnras/stac1020](https://doi.org/10.1093/mnras/stac1020)
- Laigle, C., Pichon, C., Codis, S., et al. 2015, MNRAS, 446, 2744, doi: [10.1093/mnras/stu2289](https://doi.org/10.1093/mnras/stu2289)

- Lam, R., Sanchez-Gonzalez, A., Willson, M., et al. 2022, GraphCast: Learning skillful medium-range global weather forecasting. <https://arxiv.org/abs/2212.12794>
- LeCun, Y., Boser, B., Denker, J. S., et al. 1989, *Neural Computation*, 1, 541, doi: [10.1162/neco.1989.1.4.541](https://doi.org/10.1162/neco.1989.1.4.541)
- Loh, J. M. 2008, *ApJ*, 681, 726, doi: [10.1086/588631](https://doi.org/10.1086/588631)
- Loshchilov, I., & Hutter, F. 2019, in *International Conference on Learning Representations*. <https://openreview.net/forum?id=Bkg6RiCqY7>
- Lou, Y., Caruana, R., Gehrke, J., & Hooker, G. 2013, in *Proceedings of the 19th ACM SIGKDD International Conference on Knowledge Discovery and Data Mining, KDD '13 (New York, NY, USA: Association for Computing Machinery)*, 623–631, doi: [10.1145/2487575.2487579](https://doi.org/10.1145/2487575.2487579)
- Lundberg, S., & Lee, S.-I. 2017, *A Unified Approach to Interpreting Model Predictions*. <https://arxiv.org/abs/1705.07874>
- Malavasi, N., Aghanim, N., Douspis, M., Tanimura, H., & Bonjean, V. 2020, *A&A*, 642, A19, doi: [10.1051/0004-6361/202037647](https://doi.org/10.1051/0004-6361/202037647)
- Mansfield, P., Darragh-Ford, E., Wang, Y., Nadler, E. O., & Wechsler, R. H. 2023, arXiv e-prints, arXiv:2308.10926, doi: [10.48550/arXiv.2308.10926](https://doi.org/10.48550/arXiv.2308.10926)
- Mao, Y.-Y., Zentner, A. R., & Wechsler, R. H. 2018, *MNRAS*, 474, 5143, doi: [10.1093/mnras/stx3111](https://doi.org/10.1093/mnras/stx3111)
- Mohammad, F. G., Villaescusa-Navarro, F., Genel, S., Anglés-Alcázar, D., & Vogelsberger, M. 2022, *ApJ*, 941, 132, doi: [10.3847/1538-4357/ac9f14](https://doi.org/10.3847/1538-4357/ac9f14)
- Molnar, C. 2022, *Interpretable Machine Learning*, 2nd edn. <https://christophm.github.io/interpretable-ml-book>
- Moster, B. P., Naab, T., Lindström, M., & O’Leary, J. A. 2021, *MNRAS*, 507, 2115, doi: [10.1093/mnras/stab1449](https://doi.org/10.1093/mnras/stab1449)
- Moster, B. P., Somerville, R. S., Maulbetsch, C., et al. 2010, *ApJ*, 710, 903, doi: [10.1088/0004-637X/710/2/903](https://doi.org/10.1088/0004-637X/710/2/903)
- Murphy, R., Srinivasan, B., Rao, V., & Ribeiro, B. 2019, in *Proceedings of Machine Learning Research, Vol. 97, Proceedings of the 36th International Conference on Machine Learning*, ed. K. Chaudhuri & R. Salakhutdinov (PMLR), 4663–4673. <https://proceedings.mlr.press/v97/murphy19a.html>
- Nagai, D., & Kravtsov, A. V. 2005, *ApJ*, 618, 557, doi: [10.1086/426016](https://doi.org/10.1086/426016)
- Necib, L., Ostdiek, B., Lisanti, M., et al. 2020, *Nature Astronomy*, 4, 1078, doi: [10.1038/s41550-020-1131-2](https://doi.org/10.1038/s41550-020-1131-2)
- Nelson, D., Pillepich, A., Genel, S., et al. 2015, *Astronomy and Computing*, 13, 12, doi: [10.1016/j.ascom.2015.09.003](https://doi.org/10.1016/j.ascom.2015.09.003)
- Nelson, D., Springel, V., Pillepich, A., et al. 2019, *Computational Astrophysics and Cosmology*, 6, 2, doi: [10.1186/s40668-019-0028-x](https://doi.org/10.1186/s40668-019-0028-x)
- Nori, H., Jenkins, S., Koch, P., & Caruana, R. 2019, arXiv preprint arXiv:1909.09223
- Olsen, C., & Gawiser, E. 2023, *ApJ*, 943, 30, doi: [10.3847/1538-4357/aca339](https://doi.org/10.3847/1538-4357/aca339)
- Olsen, C., Gawiser, E., Iyer, K., et al. 2021, *ApJ*, 913, 45, doi: [10.3847/1538-4357/abf3c2](https://doi.org/10.3847/1538-4357/abf3c2)
- Paszke, A., Gross, S., Massa, F., et al. 2019, *CoRR*, abs/1912.01703
- Peacock, J. A., & Smith, R. E. 2000, *MNRAS*, 318, 1144, doi: [10.1046/j.1365-8711.2000.03779.x](https://doi.org/10.1046/j.1365-8711.2000.03779.x)
- Peng, Y.-j., Lilly, S. J., Kovač, K., et al. 2010, *ApJ*, 721, 193, doi: [10.1088/0004-637X/721/1/193](https://doi.org/10.1088/0004-637X/721/1/193)
- Pfaff, T., Fortunato, M., Sanchez-Gonzalez, A., & Battaglia, P. 2021, in *International Conference on Learning Representations*. https://openreview.net/forum?id=roNqYL0_XP
- Pichon, C., Pogosyan, D., Kimm, T., et al. 2011, *MNRAS*, 418, 2493, doi: [10.1111/j.1365-2966.2011.19640.x](https://doi.org/10.1111/j.1365-2966.2011.19640.x)
- Pillepich, A., Nelson, D., Hernquist, L., et al. 2018, *MNRAS*, 475, 648, doi: [10.1093/mnras/stx3112](https://doi.org/10.1093/mnras/stx3112)
- Pillepich, A., Nelson, D., Springel, V., et al. 2019, *MNRAS*, 490, 3196, doi: [10.1093/mnras/stz2338](https://doi.org/10.1093/mnras/stz2338)
- Planck Collaboration, Ade, P. A. R., Aghanim, N., et al. 2016, *A&A*, 594, A13, doi: [10.1051/0004-6361/201525830](https://doi.org/10.1051/0004-6361/201525830)
- Pogosyan, D., Pichon, C., Gay, C., et al. 2009, *MNRAS*, 396, 635, doi: [10.1111/j.1365-2966.2009.14753.x](https://doi.org/10.1111/j.1365-2966.2009.14753.x)
- Rodriguez-Gomez, V., Genel, S., Vogelsberger, M., et al. 2015, *MNRAS*, 449, 49, doi: [10.1093/mnras/stv264](https://doi.org/10.1093/mnras/stv264)
- Rost, A., Kuchner, U., Welker, C., et al. 2021, *MNRAS*, 502, 714, doi: [10.1093/mnras/staa3792](https://doi.org/10.1093/mnras/staa3792)
- Rudin, C. 2019, *Nature Machine Intelligence*, 1, 206, doi: [10.1038/s42256-019-0048-x](https://doi.org/10.1038/s42256-019-0048-x)
- Sanchez-Gonzalez, A., Godwin, J., Pfaff, T., et al. 2020, in *Proceedings of Machine Learning Research, Vol. 119, Proceedings of the 37th International Conference on Machine Learning*, ed. H. D. III & A. Singh (PMLR), 8459–8468. <https://proceedings.mlr.press/v119/sanchez-gonzalez20a.html>
- Satorras, V. G., Hoogeboom, E., & Welling, M. 2021, 139, 9323. <https://proceedings.mlr.press/v139/satorras21a.html>
- Schlichtkrull, M., Kipf, T. N., Bloem, P., et al. 2018, in *The Semantic Web*, ed. A. Gangemi, R. Navigli, M.-E. Vidal, P. Hitzler, R. Troncy, L. Hollink, A. Tordai, & M. Alam (Cham: Springer International Publishing), 593–607
- Seabold, S., & Perktold, J. 2010, in *9th Python in Science Conference*
- Seljak, U. 2000, *MNRAS*, 318, 203, doi: [10.1046/j.1365-8711.2000.03715.x](https://doi.org/10.1046/j.1365-8711.2000.03715.x)

- Shapley, L. S. 1951, Notes on the n-Person Game – II: The Value of an n-Person Game, RAND Corporation
- Sheth, R. K., & Tormen, G. 2004, MNRAS, 350, 1385, doi: [10.1111/j.1365-2966.2004.07733.x](https://doi.org/10.1111/j.1365-2966.2004.07733.x)
- Simonyan, K., Vedaldi, A., & Zisserman, A. 2014, Deep Inside Convolutional Networks: Visualising Image Classification Models and Saliency Maps. <https://arxiv.org/abs/1312.6034>
- Somerville, R. S., & Davé, R. 2015, ARA&A, 53, 51, doi: [10.1146/annurev-astro-082812-140951](https://doi.org/10.1146/annurev-astro-082812-140951)
- Somerville, R. S., Hopkins, P. F., Cox, T. J., Robertson, B. E., & Hernquist, L. 2008, MNRAS, 391, 481, doi: [10.1111/j.1365-2966.2008.13805.x](https://doi.org/10.1111/j.1365-2966.2008.13805.x)
- Sousbie, T. 2011, MNRAS, 414, 350, doi: [10.1111/j.1365-2966.2011.18394.x](https://doi.org/10.1111/j.1365-2966.2011.18394.x)
- Springel, V., White, S. D. M., Tormen, G., & Kauffmann, G. 2001, MNRAS, 328, 726, doi: [10.1046/j.1365-8711.2001.04912.x](https://doi.org/10.1046/j.1365-8711.2001.04912.x)
- Tinker, J. L., Conroy, C., Norberg, P., et al. 2008, ApJ, 686, 53, doi: [10.1086/589983](https://doi.org/10.1086/589983)
- Vale, A., & Ostriker, J. P. 2004, MNRAS, 353, 189, doi: [10.1111/j.1365-2966.2004.08059.x](https://doi.org/10.1111/j.1365-2966.2004.08059.x)
- Villanueva-Domingo, P., & Villaescusa-Navarro, F. 2022, ApJ, 937, 115, doi: [10.3847/1538-4357/ac8930](https://doi.org/10.3847/1538-4357/ac8930)
- Villar, S., Hogg, D. W., Storey-Fisher, K., Yao, W., & Blum-Smith, B. 2021, CoRR, abs/2106.06610
- Virtanen, P., Gommers, R., Oliphant, T. E., et al. 2020, Nature Methods, 17, 261, doi: [10.1038/s41592-019-0686-2](https://doi.org/10.1038/s41592-019-0686-2)
- Wadekar, D., Villaescusa-Navarro, F., Ho, S., & Perreault-Levasseur, L. 2020, arXiv e-prints, arXiv:2012.00111, doi: [10.48550/arXiv.2012.00111](https://doi.org/10.48550/arXiv.2012.00111)
- Wang, H. Y., Mo, H. J., & Jing, Y. P. 2007, MNRAS, 375, 633, doi: [10.1111/j.1365-2966.2006.11316.x](https://doi.org/10.1111/j.1365-2966.2006.11316.x)
- Wang, K., Avestruz, C., Guo, H., Wang, W., & Wang, P. 2023, The Beyond-Halo Mass Effects of the Cosmic Web Environment on Galaxies. <https://arxiv.org/abs/2309.15306>
- Weaver, J. R., Davidzon, I., Toft, S., et al. 2023, A&A, 677, A184, doi: [10.1051/0004-6361/202245581](https://doi.org/10.1051/0004-6361/202245581)
- Wechsler, R. H., Bullock, J. S., Primack, J. R., Kravtsov, A. V., & Dekel, A. 2002, ApJ, 568, 52, doi: [10.1086/338765](https://doi.org/10.1086/338765)
- Wechsler, R. H., & Tinker, J. L. 2018, ARA&A, 56, 435, doi: [10.1146/annurev-astro-081817-051756](https://doi.org/10.1146/annurev-astro-081817-051756)
- Wechsler, R. H., Zentner, A. R., Bullock, J. S., Kravtsov, A. V., & Allgood, B. 2006, ApJ, 652, 71, doi: [10.1086/507120](https://doi.org/10.1086/507120)
- Weinmann, S. M., van den Bosch, F. C., Yang, X., & Mo, H. J. 2006, MNRAS, 366, 2, doi: [10.1111/j.1365-2966.2005.09865.x](https://doi.org/10.1111/j.1365-2966.2005.09865.x)
- Woo, J., Dekel, A., Faber, S. M., et al. 2013, MNRAS, 428, 3306, doi: [10.1093/mnras/sts274](https://doi.org/10.1093/mnras/sts274)
- Wu, J. F. 2020, ApJ, 900, 142, doi: [10.3847/1538-4357/abacbb](https://doi.org/10.3847/1538-4357/abacbb)
- Wu, J. F., & Jespersen, C. K. 2023, arXiv e-prints, arXiv:2306.12327, doi: [10.48550/arXiv.2306.12327](https://doi.org/10.48550/arXiv.2306.12327)
- Yang, X., Mo, H. J., & van den Bosch, F. C. 2003, MNRAS, 339, 1057, doi: [10.1046/j.1365-8711.2003.06254.x](https://doi.org/10.1046/j.1365-8711.2003.06254.x)
- Zehavi, I., Contreras, S., Padilla, N., et al. 2018, ApJ, 853, 84, doi: [10.3847/1538-4357/aaa54a](https://doi.org/10.3847/1538-4357/aaa54a)
- Zhang, X., Wang, Y., Zhang, W., et al. 2019, arXiv e-prints, arXiv:1902.05965, doi: [10.48550/arXiv.1902.05965](https://doi.org/10.48550/arXiv.1902.05965)
- Zheng, Z., Berlind, A. A., Weinberg, D. H., et al. 2005, ApJ, 633, 791, doi: [10.1086/466510](https://doi.org/10.1086/466510)
- Zinger, E., Dekel, A., Kravtsov, A. V., & Nagai, D. 2018, MNRAS, 475, 3654, doi: [10.1093/mnras/stx3329](https://doi.org/10.1093/mnras/stx3329)
- Zu, Y., & Mandelbaum, R. 2018, MNRAS, 476, 1637, doi: [10.1093/mnras/sty279](https://doi.org/10.1093/mnras/sty279)